Acta Geochim (2020) 39(5):668–697
https://doi.org/10.1007/s11631-020-00397-4

ORIGINAL ARTICLE

Geochronology and geochemistry of magmatic rocks in the Dongzi–Changhanboluo Pb–Zn ore district in Chifeng, Inner Mongolia, and their relationship with metallogenesis

Hongjing Xie[1] · **Yuwang Wang**[1] · **Yunguo Zhang**[2] · **Wei Jiang**[2] · **Zhiyuan Sun**[1]

Received: 28 September 2019 / Revised: 26 November 2019 / Accepted: 7 January 2020 / Published online: 17 January 2020

Abstract Bulk-rock elements, isotopes, and zircon U–Pb ages are reported for magmatic rocks in the Dongzi–Changhanboluo Pb–Zn ore district in Chifeng, Inner Mongolia, China. Zircon U–Pb dating identified four stages of magmatism: Late Silurian gabbroic diorite (∼ 420 Ma), Middle Permian monzonite (∼ 274 Ma), Late Jurassic quartz porphyry and ignimbrite, breccia tuff (153–158 Ma) and Early Cretaceous andesitic porphyrite (∼ 127 Ma). Integrating field observations, geochronology, and element and isotope geochemistry indicated a complex petrogenetic history of the magmatic rocks. The gabbroic diorite may have been sourced from EM1-type mantle. The source of the monzonite may have been mantle metasomatized by melt from the subducting plate. The Jurassic volcaniclastic rocks formed in a medium-pressure, high-temperature environment, possibly in the background of crustal thickening in a syncollisional stage and an early postcollisional stage. During this process, shaly sedimentary rocks were brought into the deep crust and heated, followed by the rapid isostatic uplift of the crust, which caused partial melting of the sedimentary rocks. Quartz monzonite porphyry and quartz porphyry formed by partial melting of mantle metasomatized by subducted sediments, but the quartz porphyry experienced high-degree differentiation and evolution. The andesitic porphyrite has characteristics similar to those of Permian monzonite, indicating that its source area was also the zone of mantle metasomatized by subducted sediment. The late Silurian and Permian magmatic rocks in this area most likely formed against a continental arc background related to the subduction of the Paleo-Asian Ocean Plate beneath the North China Plate. The Late Jurassic magmatic rocks suggest that the northern margin of the North China Craton may have been in a post-collisional setting during the Late Jurassic, with no obvious crustal thinning. The Cretaceous andesitic porphyrite may have formed against the background of lithospheric extension and thinning. According to the comprehensive analysis of geological characteristics, diagenetic and metallogenic epochs, and Pb isotope data, the formation of ore bodies in the Dongzi–Changhanboluo ore district was closely related to the Jurassic quartz porphyry.

Keywords Pb–Zn ore district · Chifeng · Zircon U–Pb dating · Sr–Nd–Pb isotope · Relationship with metallogenesis

1 Introduction

The northern margin of the North China Craton (NCC) has undergone a complicated and long-term evolutionary process, forming a variety of different types of deposits (Rui et al. 1994; Chen et al. 2003; Zhang et al. 2009a; Liu et al. 2010). The Chifeng area is located in the eastern part of the northern margin of the NCC, which hosts many gold deposits (e.g., Honghuagou and Lianhuashan), Mo deposits (e.g., Giguanshan, Nianzigou, and Chehugou), and Pb–Zn deposits (e.g., Dongzi and Xiaoyingzi) (Fig. 1b) and has become one of the most important ore clusters in eastern China. Many studies have been carried out on the Mo and Au deposits to identify the geological characteristics, ore genesis, and corresponding geodynamic settings (Qin et al.

✉ Hongjing Xie
xiehongjing717@163.com

[1] Beijing Institute of Geology and Mineral Resources, Beijing 100012, China

[2] Sinotech Mineral Exploration Co., Ltd, Beijing 100012, China

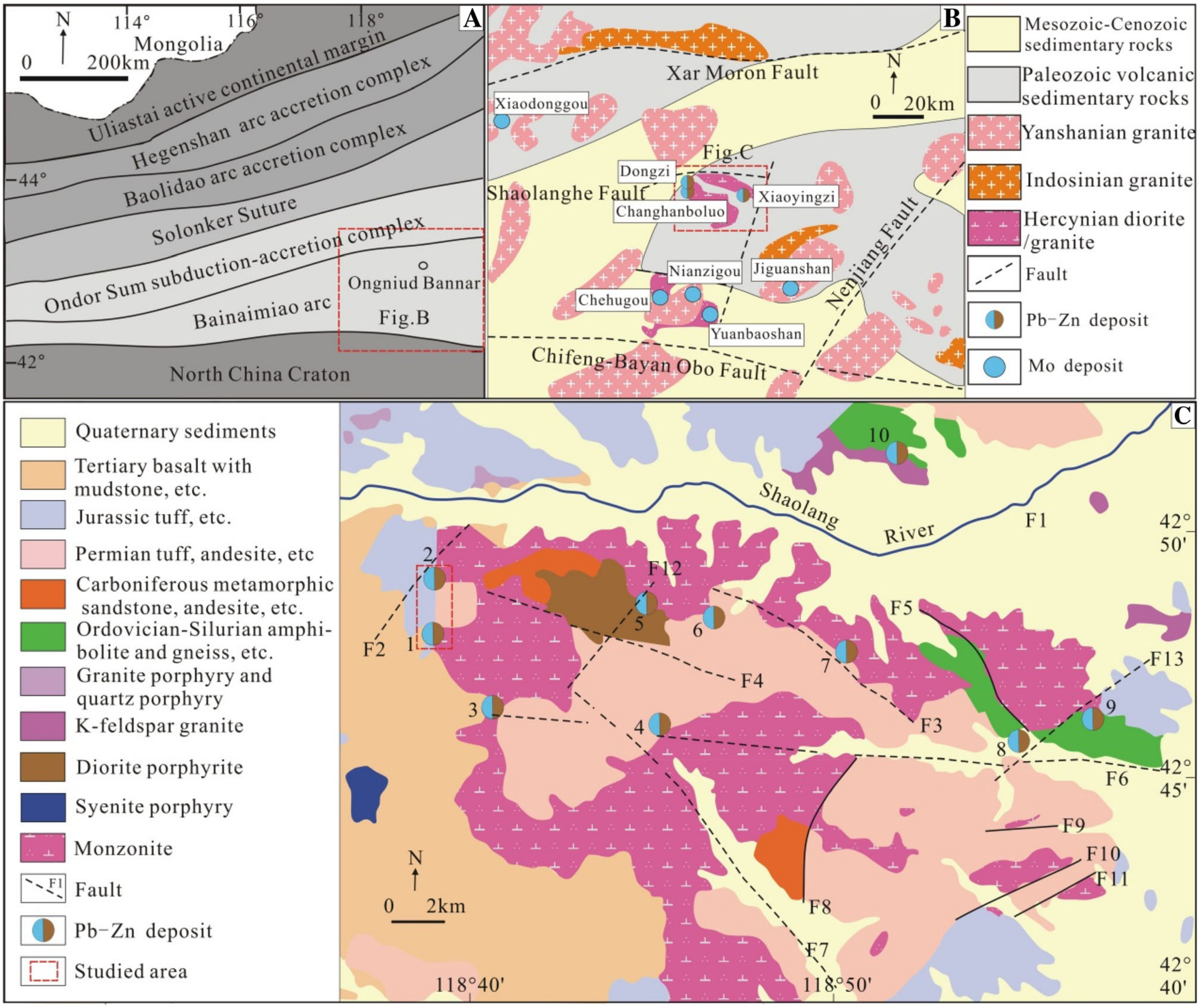

Fig. 1 Geological sketch map of the northern margin of the North China Craton, showing the location of major Mo and Pb–Zn deposits (after Liu et al. 2010). Serial numbers of Pb–Zn deposits: 1-Changhanboluo; 2-Dongzi; 3-Paoshouyingzi; 4-Shanzuizi; 5-Tianchungou; 6-Xishuiquan; 7-Dongshuiquan; 8-Xiaoyingzi; 9-Mujiadian; 10-Yujiawopu

2009; Liu et al. 2010; Zhang et al. 2010b; Sun 2013; Wu et al. 2014; Shu et al. 2015; Wang et al. 2017). However, the Pb–Zn deposits have received little attention, and only a small amount of research has been carried out (Chen et al. 2003; Tang 2013; Xie et al. 2016a, b). The Pb–Zn deposits (e.g., Dongzi, Changhanboluo, Xishuiquan, Paoshouyingzi, Xiaoyingzi, and Yujiawopu) are distributed near the Shaolang River fault, which is a secondary fault of the Xilamulun fault, and form the Shaolanghe Pb–Zn–Ag metallogenic belt (Fig. 1b).

The Dongzi and Changhanboluo deposits are located in the western part of the Shaolanghe Pb–Zn–Ag metallogenic belt and have been classified as hydrothermal vein-type deposits that formed at 153 Ma and 157.6 Ma, respectively (Chen et al. 2003; Xie et al. 2016a). Previous studies have mainly focused on the geological characteristics and ore-forming fluids, which suggest that the deposits are mostly controlled by fault structures and that the mixing of hot magmatic fluids and meteoric water resulted in the rapid precipitation of ore-forming materials (Xie et al. 2016a; Wang et al. 2017). However, note that extensive magmatic rocks are developed in the Dongzi–Changhanboluo Pb–Zn ore district. These magmatic rocks can provide important constraints on magmatic processes and tectonic settings. However, to date, the petrogenesis and tectonic settings of the magmatic rocks in this area remain poorly constrained. In addition, the period of magmatism related to mineralization is ambiguous. In this paper, we report new geochronological and geochemical data for the magmatic rocks of the Dongzi–Changhanboluo

Pb–Zn ore district in Chifeng. These results can help us better understand the timing of magmatism and Pb–Zn mineralization in this area and elucidate the petrogenesis of these intrusions and their relationship with metallogenesis.

2 Regional geological setting

The Dongzi–Changhanboluo Pb–Zn ore district belongs to the Bainaimiao arc on the northern margin of the NCC (Fig. 1a), which is bounded by the Xilamulun fault to the north and the Chifeng-Bayan Obo fault to the south. Magmatism of the Hercynian, Indosinian, and Yanshanian periods developed in much of the region, forming a large number of Mo, Pb, and Zn deposits (Fig. 1b). Some thorough and detailed studies on the Mo deposits in this area concluded that the mineralization was closely related to the synchronous intermediate-acid magmatism. The diagenesis and mineralization are mainly concentrated in the three periods of 258–210, 185–150, and 140–110 Ma, which correspond to the three processes of post-collisional extension, tectonic stress transformation, and intracontinental extension (Zhang et al. 2010a).

The Pb–Zn deposits mainly occur in the Shaolanghe Pb–Zn–Ag metallogenic belt, where more than ten small and medium-sized Pb–Zn deposits have been formed (Fig. 1c). The Dongzi and Changhanboluo deposits are located in the western part of the Shaolanghe Pb–Zn–Ag metallogenic belt. The main strata exposed in the study area include Ordovician–Silurian amphibolite and gneiss, which are scattered in the Dongzi and Yujiawopu ore districts; Carboniferous sandstone, andesite, etc.; a Permian volcanic-sedimentary clastic rock series, members of which are widely distributed and act as important host rocks; a Jurassic volcanic-sedimentary rock series, such as tuff, breccia tuff, ignimbrite, and others; and Tertiary porous and dense massive basalt with mudstone (Fig. 1c).

Fault structures are the main structural type in this area, followed by fold structures. The main fold structure is the Dongzi–Xiaoyingzi E-W-trending compound anticline, which has undergone several stages of tectono-magmatic activity. The faults in the study area are well-developed, with E-W, N-W, and N-E directions, and form a lattice fault system. The E-W-trending Shaolanghe fault and its secondary faults on both sides controlled the locations of the Pb–Zn–Ag ore veins, while the NE-trending faults controlled the distribution of magmatic rocks.

Multiple magmatic events took place in this region during different episodes, leading to the formation of the Herwusu monzonite, K-feldspar granite and granite porphyry, quartz porphyry, diorite porphyry, and syenite porphyry occurring as batholith, stocks, and dikes. The Herwusu monzonite intruded into the Permian System, and a large number of Pb–Zn deposits or ore sites are distributed around the monzonite batholith (Fig. 1c). These Pb–Zn deposits formed in the Jurassic and corresponded to the structural system transition process in the northern margin of the NCC (Rui et al. 1994; Chen et al. 2003; Wang 2016; Xie et al. 2016a).

3 Deposit geology and petrographic characteristics

The Dongzi deposit is a representative deposit of the Shaolanghe Pb–Zn–Ag metallogenic belt and was classified as an epithermal deposit in previous studies (Xie et al. 2016b). The strata in the Dongzi Pb–Zn mining area are mainly Permian andesite. The ore bodies, which lie concealed between gabbroic diorite and andesite units, are obviously controlled by faults. The main magmatic rocks are the Herwusu monzonite and the Dongzi gabbroic diorite. Some enclosed ancient amphibolite strata can also be seen in the gabbroic diorite body (Fig. 2a). There are two main ore bodies in the mining area: 1 and 1-1. The No. 1 ore body is the main E-W-trending ore body and has good continuity along a length of approximately 1530 m. The No. 1-1 ore body is a vein parallel to the No. 1 orebody, which also occurs in a vein shape. The metallic minerals are pyrite, galena, and sphalerite, followed by chalcopyrite, arsenopyrite, and others. The wall rock alteration is dominated by medium- to low-temperature linear alteration, such as silicification, sericitization, carbonation, and chloritization, which has developed on both sides of the hydrothermal vein.

The Changhanboluo deposit is located south of the Dongzi deposit (Fig. 1c). The strata that crop out in the mining area are mainly the Permian Yujiabeigou Formation andesite and andesitic basalt, which are exposed in the northeastern part of the mining area; the Jurassic Baiyingaolao Formation tuff and ignimbrite, which are widely exposed in the northwest and central parts of the mining area; and the Tertiary Hannuoba Formation basalt and mudstone, which are exposed in the middle part of the mining area (Fig. 2b). The intrusive rocks in the mining area include the Herwusu monzonite, which occurs as a batholith and overlaps the Permian andesite strata from east to west, a small number of quartz monzonitic porphyry veins filled along N-E or E-W faults, quartz porphyry intruded between the Herwusu monzonite and andesite and andesitic porphyrite veins that penetrate the quartz porphyry (Fig. 2b, c). The ore bodies lie concealed to the south of the mining area and mainly occur in quartz porphyry as veins. The main metallic minerals are galena, sphalerite, and pyrite, followed by chalcopyrite, arsenopyrite, aerosite, tetrahedrite, and others.

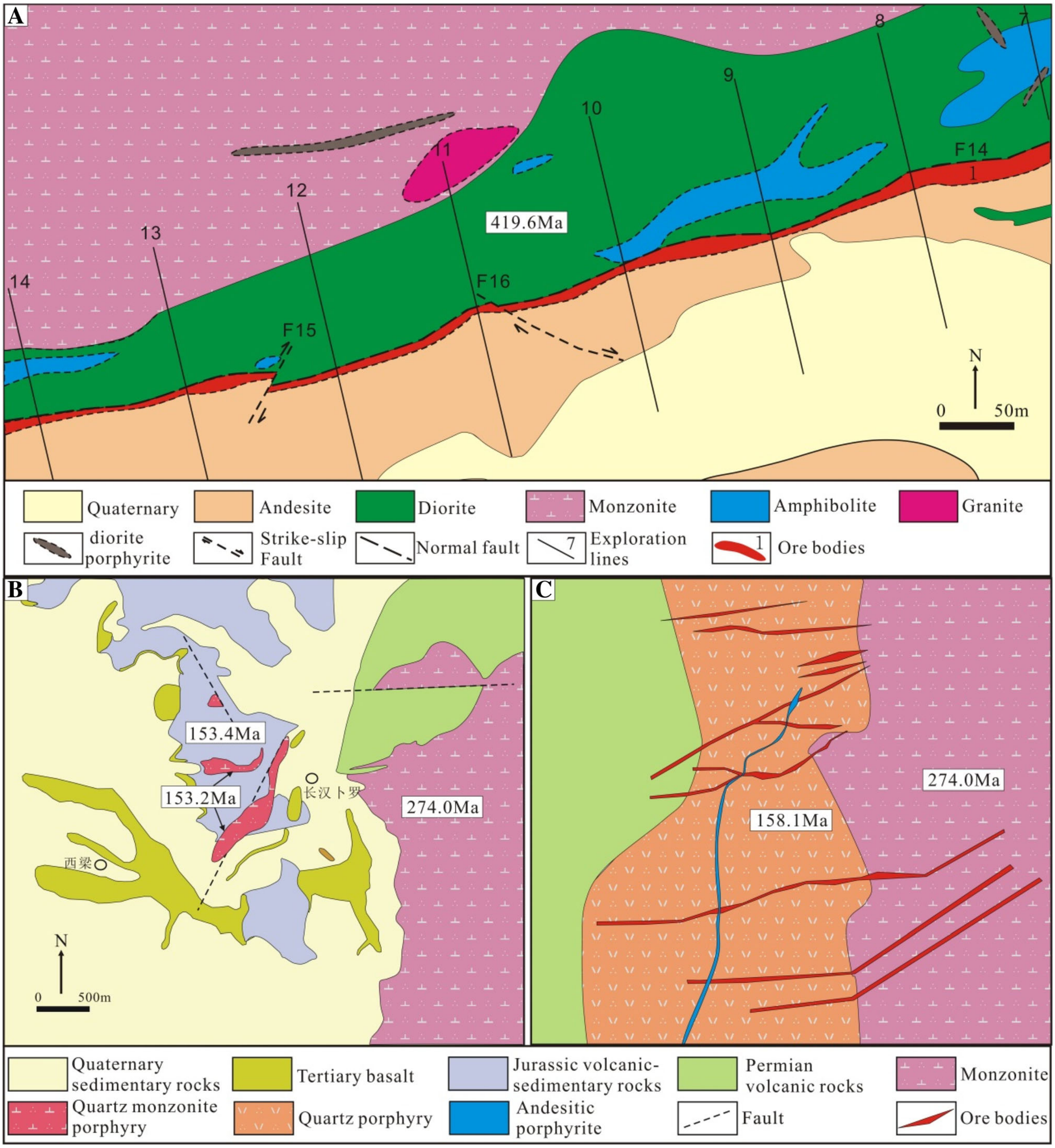

Fig. 2 Geological maps of Dongzi (**a**), the Changhanboluo ore district (**b**) and the 750 m ichnography of the Changhanboluo mining area (**c**)

Extensive magmatic activity occurred in the Dongzi–Changhanboluo ore district and formed various rock types, which are mainly composed of the Dongzi gabbroic diorite, Herwusu monzonite, Changhanboluo quartz porphyry, and andesite porphyrite. In addition, there are some volcaniclastic rocks, such as ignimbrite and breccia tuff in the northwestern part of the Changhanboluo mining area, which are intruded by quartz monzonite porphyry veins.

The Dongzi gabbroic diorite and andesite are the main host rocks of the ore bodies, and we can see some hydrothermal veins intruded into the andesite (Fig. 3a). The Dongzi gabbroic diorite is a medium-grained rock with a hypidiomorphic granular texture (Fig. 3d). The rock is

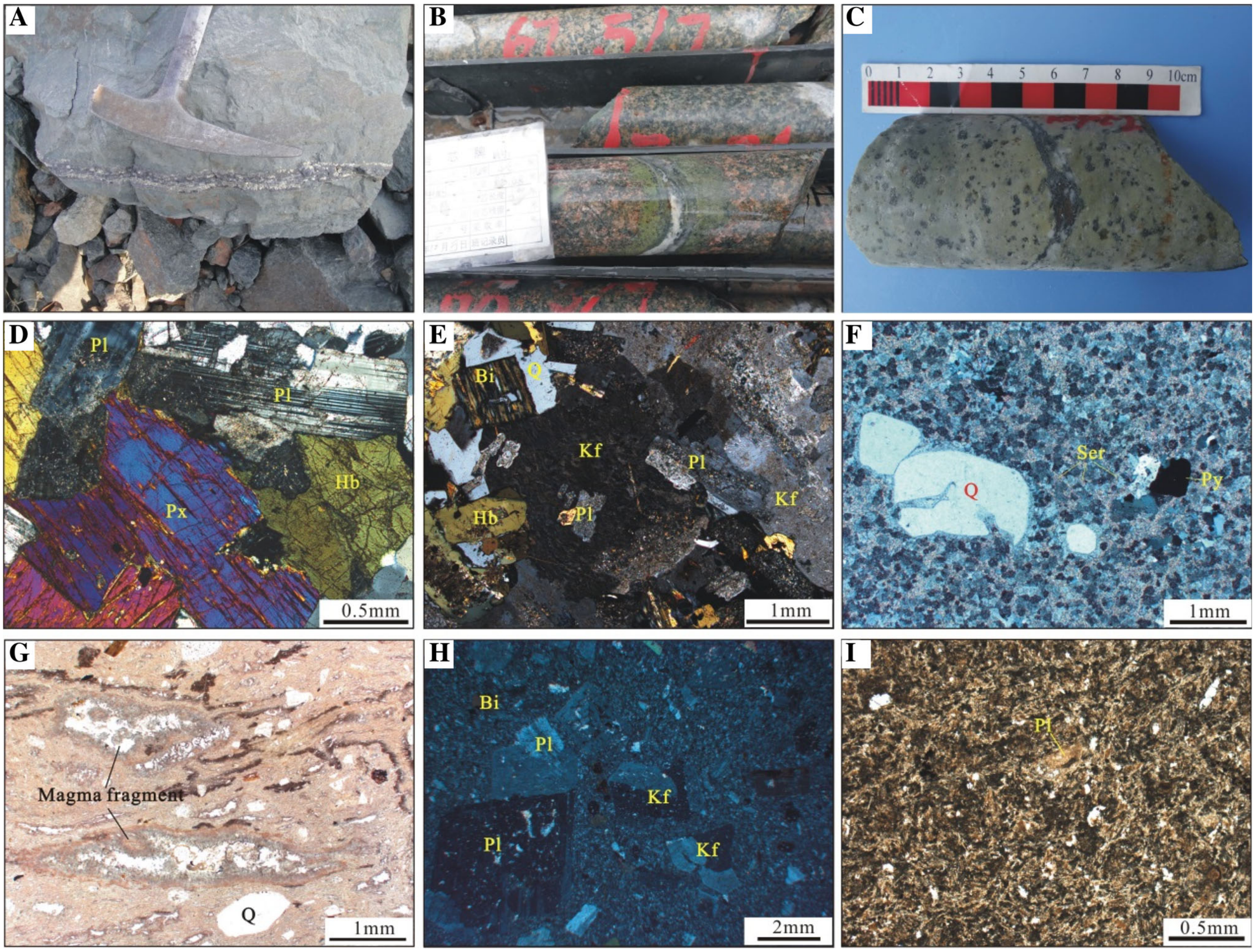

Fig. 3 Field photographs and photomicrographs of magmatic rocks in the Dongzi–Changhanboluo ore district. **a** Dongzi hydrothermal veins penetrated fractures in andesite; **b** Changhanboluo ore veins penetrated fractures in monzonite and caused chlorite alteration; **c** quartz porphyry with disseminated mineralization and hydrothermal vein penetration; **d** Dongzi gabbroic diorite; **e** Herwusu monzonite; **f** quartz porphyry; **g** rhyolite ignimbrite; **h** quartz monzonite porphyry; **i** andesitic porphyrite. Mineral abbreviations: Bi, biotite; Hb, hornblende; Kf, K-feldspar; Pl, plagioclase; Px, pyroxene; Py, pyrite; Q, quartz; Ser, sericite. **a** The Dongzi gabbroic diorite (DZ18-1); **b** the Herwusu monzonite (Zk003-104.5); **c1**, **c2** the quartz porphyry (CHBL-1); **d** the ignimbrite (BD-10); **e** the quartz monzonite porphyry (BD-23); **f**, **g** the andesitic porphyrite (CH-CM-2)

composed of plagioclase (~ 70 vol%), pyroxene (~ 15 vol%), and hornblende (~ 12 vol%), with minor amounts of quartz and apatite (~ 3 vol%). The plagioclase is plate-shaped, measures 0.2 × 1.0–0.6 × 2.0 mm, and forms subhedral laths with occasional albite and Carlsbad-albite-type combined twinning. The pyroxene and hornblende are idiomorphic–hypidiomorphic granular with granularities between 0.3 and 1.5 mm.

The Herwusu monzonite are fresh and there are also hydrothermal veins penetrating into the monzonite (Fig. 3b). The monzonite displays a monzonitic texture composed of plagioclase (~ 40 vol%), K-feldspar (~ 40 vol%) and minor quartz (~ 5 vol%), amphibole (~ 8 vol%), and biotite (~ 6 vol%). The accessory minerals are apatite, titanite, zircon, etc. (Figure 3e). The K-feldspars have xenomorphic granular textures and are mostly altered to kaolinite. The plagioclases are euhedral and tabular, measuring 0.8 × 1.6–1.6 × 3.2 mm, with polysynthetic twins and zoned textures, and a portion are replaced by sericite. Anhedral plagioclase is embedded in the K-feldspar crystals.

The quartz porphyry invaded between the andesite and the Herwusu monzonite as stocks, and it often shows disseminated mineralization with hydrothermal vein penetration (Fig. 3c). The rock has a porphyritic texture, with quartz as the phenocrysts. The quartz phenocrysts (~ 30 vol%) occur with a xenomorphic granular texture, measure 0.4–2.4 mm in diameter and are mostly eroded, with embayed shapes. The matrix is composed of felsic minerals with spherulitic textures and is generally altered to sericite.

The rhyolite ignimbrite shows a welded tuff texture and pseudo flow structures and is composed of a large number of rock fragments (~ 60 vol%), vitroclastic fragments (~ 25 vol%), and a small amount of crystal fragments (~ 15 vol%). The rock fragments are banded and flame-like at both ends and show the same direction as that of the vitroclastic fragments, which look like fine stripes and earthworms. The crystal fragments are mainly composed of quartz, plagioclase, biotite, etc. (Fig. 3g).

The Changhanboluo quartz monzonite porphyry shows a porphyritic texture and contains ~ 60 vol% phenocrysts by volume (Fig. 3h). The phenocrysts consist of platy plagioclase (~ 35 vol%), K-feldspar (~ 20 vol%), and subordinate biotite (~ 5 vol%). The plagioclase phenocrysts generally form subhedral laths with occasional albite and Carlsbad-albite-type combined twinning. Some of these laths display distinct zoning. The K-feldspar is mostly granular, and some are metasomatized to chlorite in the middle. The biotite is reddish-brown, indicating high Ti content, and some are decomposed to form rutile.

The andesitic porphyrite invaded the quartz porphyry as veins, with obvious differences in occurrence. The rock is porphyritic with an almond structure. The phenocrysts and matrix are plagioclase and elongated plagioclase microlites, respectively (Fig. 3i).

4 Samples and analytical methods

4.1 Zircon U–Pb dating

Zircons for U–Pb dating were selected from the magmatic rocks of the Dongzi–Changhanboluo ore district (Dongzi diorite DZ18-1; Changhanboluo quartz monzonite Zk003-104.5; ignimbrite BD-10; quartz monzonite porphyry BD-23; andesite porphyry CH-CM-2 and quartz porphyry CHBL-1). These zircons were separated using conventional heavy liquid and magnetic techniques and then handpicked under a binocular microscope to select euhedral and translucent zircons for analysis. The zircons were mounted in epoxy and then polished and gold-coated for subsequent cathodoluminescence (CL) imaging and zircon U–Pb analyses. CL images were obtained at the Electron Microprobe Laboratory of the Institute of Geology, Chinese Academy of Geological Sciences (CAGS). Two methods, laser-ablation inductively coupled plasma mass spectrometry (LA-ICP-MS) and secondary-ion mass spectrometry (SIMS), were used for zircon U–Pb dating.

LA-ICP-MS analyses were performed on the exposed zircon surfaces using a 213 laser ablation system coupled with an Agilent 7500a quadrupole ICP-MS instrument at the Key Laboratory of Orogenic Belt and Crustal Evolution, Beijing University, China. The zircon standard PLE was used as a calibration standard, while the zircon standard QH was used as a supplementary calibration standard. The laser beam had a diameter of 32–60 μm, depending on the sample grain size, was operated at 5 Hz and 12 J/cm^2 and was limited to an analytical cycle of 0.2 s. Ages were calculated from the U and Th decay constants recommended by Steiger and Jäger (1977). All data were processed using the Glitter 4.4 software, and the reported ages were calculated using Isoplot 3.0.

SIMS zircon U–Pb analyses were conducted using the CAMECA IMS-1280 ion microprobe at the Institute of Geology and Geophysics, Chinese Academy of Sciences, Beijing, China. U–Th–Pb ratios and absolute abundances were determined relative to the zircon standard 91500 (Wiedenbeck et al. 1995), and the instrumental performance and detailed analytical procedures were similar to those described by Li et al. (2009). Isotopic compositions were corrected for common Pb using the measured ^{204}Pb. Uncertainties concerning individual analyses in data tables are reported at the 1σ level and mean ages for pooled U/Pb analyses are quoted at the 95 % confidence interval. Data reduction was performed using Isoplot 3.0 (Ludwig 2003).

4.2 Major and trace element determinations

The major and trace element compositions were determined at the Analytical Laboratory of the Beijing Research Institute of Uranium Geology, China National Nuclear Corporation (CNNC). The major element compositions were analyzed using an automatic X-ray fluorescence (XRF) spectrometer (Philips PW2404). The contents of volatiles (e.g., CO_2 and H_2O) were determined by measuring the reduction in weight that resulted after heating the samples at 1050 °C for 30 min. The analytical precision for the major oxides SiO_2, Al_2O_3, MgO, CaO, and TFe_2O_3 was better than 0.1 wt%, and that for the major oxides MnO, Na_2O, K_2O, P_2O_5,and TiO_2 was better than 0.01 wt%. Trace elements, including rare earth elements (REEs), were determined using an ELEMENT ICP-MS. The measurement precision for the trace elements was generally better than 3 wt%.

4.3 Sr–Nd–Pb isotope analysis

The Sr–Nd–Pb isotope analyses were conducted using an ISOPROBE-T thermoelectric ionization mass spectrometer (TIMS) at the Analytical Laboratory of the Beijing Research Institute of Uranium Geology, CNNC. The Sr–Nd isotopic ratios were corrected for mass fractionation by normalization to $^{86}Sr/^{88}Sr = 0.1194$ and $^{146}Nd/^{144}Nd = 0.7219$. The international standard samples NBS-987 and JMC were employed to evaluate the instrument stability during the period of data collection. The measured values for the NBS-987 Sr standard and the JMC Nd standard were

$^{87}Sr/^{86}Sr$ = 0.710250 ± 7 (2SD) and $^{143}Nd/^{144}Nd$ = 0.512109 ± 3 (2SD), respectively. The Pb isotopic analytical procedures were described by Liu et al. (2014). The analytical precision was 0.005% for $^{208}Pb/^{206}Pb$.

5 Results

5.1 Zircon U–Pb dating

Zircon U–Pb dating of samples from the Dongzi deposit (sample DZ18-1) and Changhanboluo deposit (samples Zk003-104.5, BD-10, BD-23, and CH-CM-2) was undertaken using LA-ICP-MS, whereas zircons of sample CHBL-1 from the Changhanboluo deposit were analyzed using SIMS U–Pb dating because of the small size of the zircon particles. The results are given in Table 1 and shown in Fig. 4.

5.1.1 The Dongzi gabbroic diorite

Sample DZ18-1 is a gabbroic diorite collected from the Dongzi deposit. Zircons from this sample are short columnar or long columnar, with particle sizes varying from 50 to 300 μm, and the ratio of the long to the short axis is mostly between 1:1 and 3:1. The zircons have oscillatory growth zoning, which is typical of magmatic zircons (Koschek 1993). The $^{206}Pb/^{238}U$ ages from 20 zircon analyses yield a weighted mean $^{206}Pb/^{238}U$ age of 419.6 ± 5.5 Ma [mean square weighted deviation (MSWD) = 1.16] (Fig. 4a), representing the emplacement age of the gabbroic diorite.

5.1.2 The Herwusu monzonite

Sample Zk003-104.5 is a monzonite collected from drill core Zk003 in the Changhanboluo deposit. This sample yields euhedral zircons with oscillatory growth zoning and Th/U ratios of 0.91–1.89, which are indicative of an igneous origin (Koschek 1993; Hoskin and Black 2000). The $^{206}Pb/^{238}U$ ages obtained from 25 analyses range between 270 and 276 Ma, yielding a weighted mean $^{206}Pb/^{238}U$ age of 274.0 ± 1.0 Ma (MSWD = 0.33) (Fig. 4b), which is interpreted to represent the formation time of the monzonite.

5.1.3 The quartz porphyry

Sample CHBL-1 is a quartz porphyry collected from the tunnel of the Changhanboluo deposit. Zircons from this sample are euhedral-subhedral with oscillatory growth zoning and have high Th/U ratios (0.13–1.05), suggesting a magmatic origin (Hoskin and Black 2000). The $^{206}Pb/^{238}U$ ages from 19 zircon analyses range from 149 to 240 Ma, yielding two concordant groups of ages at 229.8 ± 6.3 Ma (MSWD = 4.3, n = 11) and 158.1 ± 3.4 Ma (MSWD = 4.0, n = 8) (Fig. 4c1, c2). These data indicate that the quartz porphyry formed at 158.1 ± 3.4 Ma, with 229.8 ± 6.3 Ma representing the age of captured or inherited zircons entrained by the quartz porphyry.

5.1.4 The ignimbrite and quartz monzonite porphyry

Samples BD-10 and BD-23 are an ignimbrite and a quartz monzonite porphyry, respectively, collected from the western part of the Dongzi–Changhanboluo ore district and contain euhedral–subhedral zircons with oscillatory zoning that have Th/U ratios of 0.39–7.37, indicating a magmatic origin (Koschek 1993; Hoskin and Black 2000). The $^{206}Pb/^{238}U$ ages from the zircon analyses of ignimbrite and quartz monzonite porphyry yield weighted mean $^{206}Pb/^{238}U$ ages of 153.4 ± 0.7 Ma (MSWD = 1.2) and 153.2 ± 0.7 Ma (MSWD = 1.0) (Fig. 4d, e), respectively, which are interpreted as the crystallization ages of the ignimbrite and quartz monzonite porphyry.

5.1.5 The andesitic porphyrite

Sample CH-CM-2 collected from the tunnel of the Changhanboluo deposit is an andesitic porphyrite that cuts through the Changhanboluo Pb–Zn ore veins. Zircons from this sample are subhedral with oscillatory zoning and have high Th/U ratios (0.43–1.08), suggesting a magmatic origin (Hoskin and Black 2000). The $^{206}Pb/^{238}U$ ages from 10 analyses yield a weighted mean $^{206}Pb/^{238}U$ age of 127.4 ± 1.9 Ma (MSWD = 4.7) (Fig. 4f, g), which is interpreted as the crystallization age of the andesitic porphyrite. Most of the other analyses show the occurrence of Pb loss and may not be significant.

The above zircon U–Pb ages suggest that the Early Paleozoic–Mesozoic magmatism in the study area can be subdivided into four stages: Late Silurian (~ 420 Ma), Middle Permian (~ 274 Ma), Late Jurassic (153–158 Ma) and Early Cretaceous (~ 127 Ma).

5.2 Major and trace elements

The major and trace element geochemistry of the Early Paleozoic–Mesozoic magmas of the Dongzi–Changhanboluo ore district is given in Table 2.

5.2.1 Late Silurian magmas

The Late Silurian magmas in the study area are the Dongzi gabbroic diorites. They have SiO_2 = 50.77–52.88 wt%, TiO_2 = 0.73–0.85 wt%, Al_2O_3 = 19.72–20.14 wt%, $Mg^{\#}$

Table 1 LA–ICP–MS and SIMS zircon U–Pb data for magmatic rocks from the Dongzi–Changhanboluo ore district

No.	Element(ppm)			Th/U	Isotope ratio						Apparent age (Ma)					
	Pb	U	Th		^{206}Pb/^{238}U	1σ	^{207}Pb/^{235}U	1σ	^{207}Pb/^{206}Pb	1σ	^{206}Pb/^{238}U	1σ	^{207}Pb/^{235}U	1σ	^{207}Pb/^{206}Pb	1σ
DZ18-1 diorite																
1	8	85	112	1.31	0.00194	0.25841	0.05936	0.06566	0.06078	0.00808	410	12	425	40	632	289
2	4	42	45	1.07	0.00199	0.27812	0.05316	0.06569	0.05696	0.00771	410	12	403	36	500	299
3	9	88	112	1.28	0.00151	0.23076	0.04945	0.06715	0.05495	0.00521	419	9	417	33	409	213
4	2	27	23	0.88	0.00261	0.29812	0.06698	0.06691	0.06277	0.01087	418	16	420	45	702	376
5	6	69	81	1.18	0.00145	0.25666	0.04250	0.06494	0.05548	0.00546	406	9	404	29	432	222
6	2	20	14	0.69	0.00264	0.30246	0.06594	0.06532	0.05824	0.01045	408	16	407	45	539	400
7	5	53	59	1.11	0.00172	0.25851	0.05129	0.07003	0.05753	0.00661	436	10	438	34	522	256
8	5	56	63	1.13	0.00218	0.39781	0.04213	0.06915	0.07117	0.01430	431	13	432	28	962	420
9	5	52	58	1.10	0.00220	0.37702	0.04494	0.06747	0.06016	0.00678	421	13	424	30	609	244
10	7	73	86	1.18	0.00154	0.31072	0.03757	0.06311	0.05771	0.00532	395	9	397	26	520	204
11	4	40	39	0.98	0.00206	0.29859	0.05242	0.06919	0.05743	0.00618	431	12	429	35	509	237
12	4	43	43	1.02	0.00177	0.27559	0.05660	0.06792	0.06620	0.00748	424	11	476	36	813	233
13	5	50	55	1.10	0.00160	0.25101	0.04826	0.06780	0.05723	0.00658	423	10	420	32	502	256
14	6	60	70	1.17	0.00142	0.24207	0.04450	0.06815	0.05643	0.00532	425	9	422	30	478	205
15	3	29	27	0.93	0.00316	0.29591	0.08223	0.07091	0.06312	0.01309	442	19	442	54	722	452
16	7	75	89	1.19	0.00157	0.27454	0.04372	0.06673	0.05738	0.00592	416	9	419	29	506	229
17	3	32	31	0.99	0.00188	0.18932	0.07600	0.06724	0.05824	0.00753	420	11	422	51	539	285
18	10	100	137	1.37	0.00141	0.25790	0.04207	0.06680	0.05623	0.00513	417	9	420	28	461	199
19	5	53	59	1.11	0.00206	0.37615	0.04277	0.07041	0.05982	0.00679	439	12	444	28	598	247
20	3	35	34	0.99	0.00191	0.26345	0.05642	0.06972	0.05721	0.00687	434	12	440	37	498	267
Zk003-104.5 quartz monzonite																
1	13	262	257	0.98	0.04330	0.00042	0.31598	0.00877	0.05292	0.00143	273	3	279	8	325	61
2	34	621	836	1.35	0.04367	0.00041	0.31272	0.00511	0.05193	0.00079	276	3	276	5	282	35
3	15	286	330	1.15	0.04367	0.00041	0.31263	0.00792	0.05192	0.00126	276	3	276	7	282	56
4	38	700	902	1.29	0.04309	0.00041	0.31589	0.00478	0.05317	0.00074	272	3	279	4	336	31
5	44	740	1332	1.80	0.04357	0.00041	0.31283	0.00494	0.05208	0.00075	275	3	276	4	289	33
6	10	210	195	0.93	0.04310	0.00042	0.31392	0.01072	0.05283	0.00177	272	3	277	9	321	76
7	10	193	188	0.97	0.04343	0.00042	0.31281	0.00986	0.05224	0.00160	274	3	276	9	296	70
8	35	692	935	1.35	0.04319	0.00041	0.31791	0.00496	0.05339	0.00076	273	3	280	4	345	32
9	36	637	957	1.50	0.04303	0.00041	0.30811	0.00481	0.05194	0.00073	272	3	273	4	283	32
10	52	907	1353	1.49	0.04285	0.00040	0.30920	0.00437	0.05233	0.00067	270	3	274	4	300	29
11	55	1003	1321	1.32	0.04288	0.00041	0.30561	0.00421	0.05169	0.00064	271	3	271	4	272	28
12	29	526	672	1.28	0.04329	0.00041	0.30870	0.00543	0.05171	0.00086	273	3	273	5	273	38
13	68	1076	2033	1.89	0.04334	0.00041	0.30857	0.00432	0.05163	0.00064	274	3	273	4	269	29
14	61	1129	1241	1.10	0.04355	0.00042	0.31059	0.00424	0.05173	0.00063	275	3	275	4	273	28
15	65	1100	1688	1.53	0.04312	0.00041	0.30780	0.00440	0.05178	0.00066	272	3	272	4	276	29

Table 1 continued

No.	Element(ppm)			Th/U	Isotope ratio						Apparent age (Ma)					
	Pb	U	Th		$^{206}Pb/^{238}U$	1σ	$^{207}Pb/^{235}U$	1σ	$^{207}Pb/^{206}Pb$	1σ	$^{206}Pb/^{238}U$	1σ	$^{207}Pb/^{235}U$	1σ	$^{207}Pb/^{206}Pb$	1σ
16	65	1200	1349	1.12	0.04359	0.00042	0.31391	0.00450	0.05222	0.00065	275	3	277	4	295	28
17	18	330	362	1.10	0.04353	0.00042	0.31607	0.00687	0.05266	0.00109	275	3	279	6	314	47
18	40	709	963	1.36	0.04329	0.00041	0.31063	0.00472	0.05205	0.00071	273	3	275	4	287	31
19	68	1288	1283	1.00	0.04356	0.00042	0.31293	0.00423	0.05210	0.00063	275	3	276	4	290	28
20	57	972	1482	1.52	0.04344	0.00042	0.31010	0.00438	0.05177	0.00065	274	3	274	4	275	29
21	48	891	992	1.11	0.04341	0.00041	0.31709	0.00460	0.05298	0.00070	274	3	280	4	328	30
22	62	1205	1158	0.96	0.04320	0.00041	0.31558	0.00443	0.05298	0.00067	273	3	279	4	328	29
23	13	251	235	0.94	0.04327	0.00042	0.31565	0.00876	0.05290	0.00142	273	3	279	8	325	61
24	34	612	806	1.32	0.04361	0.00042	0.31993	0.00497	0.05320	0.00075	275	3	282	4	337	32
25	51	992	900	0.91	0.04359	0.00042	0.31880	0.00440	0.05305	0.00065	275	3	281	4	331	28
BD-10 ignimbrite																
1	7	259	255	0.99	0.02390	0.00023	0.16667	0.00644	0.05057	0.00192	152	1	157	6	221	88
2	4	114	162	1.42	0.02371	0.00026	0.16379	0.01423	0.05009	0.00436	151	2	154	13	199	202
3	11	339	641	1.89	0.02378	0.00023	0.16507	0.00607	0.05034	0.00181	152	1	155	6	211	83
4	3	97	45	0.46	0.02421	0.00033	0.16691	0.02295	0.04999	0.00709	154	2	157	22	195	330
5	22	563	1661	2.95	0.02382	0.00023	0.16221	0.00339	0.04939	0.00098	152	1	153	3	166	46
6	10	304	514	1.69	0.02441	0.00024	0.16938	0.00527	0.05032	0.00154	155	2	159	5	210	71
7	25	664	1737	2.62	0.02370	0.00023	0.16578	0.00345	0.05074	0.00099	151	1	156	3	229	45
8	8	327	179	0.55	0.02428	0.00025	0.16888	0.00607	0.05045	0.00174	155	2	158	6	216	80
9	13	198	1461	7.37	0.02440	0.00025	0.17322	0.00868	0.05149	0.00255	155	2	162	8	263	114
10	24	615	1727	2.81	0.02440	0.00023	0.16900	0.00391	0.05023	0.00113	155	1	159	4	206	52
11	17	620	510	0.82	0.02440	0.00023	0.16555	0.00338	0.04920	0.00096	155	1	156	3	158	46
12	7	256	321	1.26	0.02390	0.00024	0.16353	0.00562	0.04962	0.00167	152	1	154	5	177	79
13	13	407	779	1.92	0.02404	0.00024	0.16638	0.00449	0.05020	0.00130	153	2	156	4	204	60
14	6	203	232	1.14	0.02439	0.00024	0.17002	0.00960	0.05055	0.00282	155	2	159	9	220	129
15	6	209	242	1.16	0.02436	0.00025	0.16401	0.00956	0.04882	0.00282	155	2	154	9	139	136
16	18	517	1119	2.17	0.02410	0.00024	0.16376	0.00357	0.04929	0.00105	153	2	154	3	162	50
17	8	254	408	1.60	0.02390	0.00025	0.16212	0.01018	0.04920	0.00303	152	2	153	10	157	144
18	21	876	386	0.44	0.02380	0.00023	0.16155	0.00303	0.04923	0.00087	152	1	152	3	159	42
19	27	524	2872	5.48	0.02424	0.00024	0.16747	0.00366	0.05010	0.00107	154	2	157	3	200	50
20	8	236	432	1.83	0.02412	0.00024	0.16566	0.00665	0.04982	0.00193	154	2	156	6	186	90
21	10	306	492	1.61	0.02419	0.00024	0.16524	0.00564	0.04955	0.00163	154	2	155	5	174	77
22	10	354	248	0.70	0.02365	0.00029	0.22922	0.00918	0.07031	0.00269	151	2	210	8	937	79
23	10	314	366	1.17	0.02436	0.00024	0.16861	0.00682	0.05019	0.00195	155	2	158	6	204	90
24	6	230	157	0.68	0.02433	0.00027	0.16767	0.01015	0.04999	0.00306	155	2	157	10	195	142

Table 1 continued

No.	Element(ppm)			Th/U	Isotope ratio						Apparent age (Ma)					
	Pb	U	Th		$^{206}Pb/^{238}U$	1σ	$^{207}Pb/^{235}U$	1σ	$^{207}Pb/^{206}Pb$	1σ	$^{206}Pb/^{238}U$	1σ	$^{207}Pb/^{235}U$	1σ	$^{207}Pb/^{206}Pb$	1σ
25	9	378	146	0.39	0.02371	0.00023	0.16645	0.00439	0.05092	0.00128	151	1	156	4	237	58
BD-23 quartz monzonite porphyry																
1	11	337	501	1.49	0.02375	0.00023	0.16571	0.00496	0.0506	0.00148	151	1	156	3	222	68
2	2	72	104	1.44	0.02387	0.00031	0.16770	0.02697	0.05095	0.00849	152	2	157	25	239	384
3	3	92	128	1.39	0.02396	0.00029	0.16460	0.02247	0.04983	0.00693	153	2	155	21	187	324
4	3	117	135	1.15	0.02374	0.00027	0.16343	0.01737	0.04993	0.00532	151	2	154	16	192	248
5	3	93	149	1.61	0.02379	0.00028	0.16552	0.02061	0.05047	0.00641	152	2	156	19	217	294
6	2	75	95	1.27	0.02378	0.00029	0.16537	0.02467	0.05043	0.00763	152	2	155	23	215	351
7	2	67	72	1.08	0.02369	0.00034	0.16412	0.03623	0.05023	0.01185	151	2	154	34	206	547
8	2	66	87	1.31	0.02427	0.00041	0.16941	0.02918	0.05063	0.00887	155	3	159	27	224	405
9	1	49	55	1.12	0.02403	0.00041	0.16884	0.03595	0.05095	0.01315	153	3	158	34	239	595
10	10	398	217	0.55	0.02437	0.00025	0.16517	0.00661	0.04916	0.00187	155	2	155	6	156	89
11	15	444	911	2.05	0.02370	0.00023	0.16800	0.00643	0.05141	0.00194	151	1	158	6	259	87
12	5	147	187	1.27	0.02380	0.00032	0.16890	0.03106	0.05146	0.00901	152	2	158	29	262	402
13	9	331	196	0.59	0.02453	0.00025	0.16868	0.00848	0.04987	0.00248	156	2	158	8	189	116
14	4	121	179	1.47	0.02397	0.00027	0.17084	0.01559	0.05170	0.00471	153	2	160	15	272	209
15	13	374	650	1.74	0.02411	0.00024	0.17012	0.00510	0.05118	0.00149	154	1	160	5	249	67
16	2	61	85	1.39	0.02414	0.00034	0.16636	0.03551	0.04998	0.01104	154	2	156	33	194	514
17	2	77	82	1.06	0.02452	0.00035	0.16610	0.03042	0.04913	0.00934	156	2	156	29	154	445
18	5	203	104	0.51	0.02454	0.00028	0.16577	0.01222	0.04900	0.00362	156	2	156	11	148	173
19	2	71	67	0.93	0.02437	0.00032	0.16907	0.01564	0.05031	0.00476	155	2	159	15	209	219
20	3	105	121	1.16	0.02426	0.00027	0.17023	0.01686	0.05089	0.00501	155	2	160	16	236	227
21	4	133	143	1.08	0.02401	0.00027	0.16426	0.01505	0.04961	0.00455	153	2	154	14	177	214
22	2	75	87	1.15	0.02426	0.00034	0.17130	0.02609	0.05121	0.00806	155	2	161	24	250	362
23	6	206	359	1.75	0.02384	0.00024	0.16442	0.00914	0.05003	0.00273	152	2	155	9	196	127
CH-CM-2 andesite porphyry																
1	36	637	391	0.61	0.05286	0.00050	0.43367	0.00688	0.05950	0.00086	332	3	366	6	586	31
2	7	342	254	0.74	0.02044	0.00020	0.13668	0.00518	0.04851	0.00181	130	1	130	5	124	88
3	10	470	271	0.58	0.02013	0.00019	0.14141	0.00436	0.05094	0.00153	128	1	134	4	238	69
4	15	726	433	0.60	0.01918	0.00018	0.13801	0.00344	0.05219	0.00124	122	1	131	3	294	54
5	7	309	264	0.85	0.01999	0.00020	0.14373	0.00963	0.05214	0.00329	128	1	136	9	292	144
6	14	533	438	0.82	0.02302	0.00022	0.21202	0.00596	0.06679	0.00171	147	1	195	5	831	53
7	7	305	256	0.84	0.02024	0.00020	0.14035	0.00626	0.05029	0.00219	129	1	133	6	208	101
8	7	304	227	0.75	0.02011	0.00020	0.13608	0.00657	0.04908	0.00236	128	1	130	6	152	112
9	19	276	155	0.56	0.06550	0.00063	0.56879	0.00989	0.06298	0.00101	409	4	457	8	708	34
10	9	273	295	1.08	0.02296	0.00022	0.46838	0.00923	0.14797	0.00272	146	1	390	8	2323	31
11	39	695	542	0.78	0.05234	0.00050	0.41487	0.00593	0.05749	0.00074	329	3	352	5	510	28

Table 1 continued

No.	Element(ppm)			Th/U	Isotope ratio						Apparent age (Ma)					
	Pb	U	Th		$^{206}Pb/^{238}U$	1σ	$^{207}Pb/^{235}U$	1σ	$^{207}Pb/^{206}Pb$	1σ	$^{206}Pb/^{238}U$	1σ	$^{207}Pb/^{235}U$	1σ	$^{207}Pb/^{206}Pb$	1σ
12	9	395	369	0.93	0.02007	0.00020	0.14020	0.00512	0.05066	0.00179	128	1	133	5	226	82
13	7	301	273	0.91	0.01982	0.00020	0.13927	0.00823	0.05096	0.00295	127	1	132	8	239	134
14	49	948	637	0.67	0.04965	0.00047	0.35811	0.00528	0.05231	0.00069	312	3	311	5	299	30
15	7	353	278	0.79	0.01937	0.00019	0.13556	0.00491	0.05075	0.00183	124	1	129	5	229	83
16	78	1459	1183	0.81	0.04984	0.00048	0.45495	0.00616	0.06620	0.00080	314	3	381	5	813	25
17	22	498	300	0.60	0.04350	0.00041	0.30887	0.00541	0.05150	0.00084	274	3	273	5	263	37
18	49	850	542	0.64	0.05263	0.00051	0.56980	0.00849	0.07853	0.00100	331	3	458	7	1160	25
19	14	643	452	0.70	0.02043	0.00020	0.14064	0.00354	0.04993	0.00120	130	1	134	3	192	56
	Pb	U	Th	Th/U	$^{206}Pb/^{238}U$	%	$^{207}Pb/^{235}U$	%	$^{207}Pb/^{206}Pb$	%	$^{206}Pb/^{238}U$	1σ	$^{207}Pb/^{235}U$	1σ	$^{207}Pb/^{206}Pb$	1σ
CHBL-1 quartz porphyry																
1	5	137	159	0.86	0.02510	1.69	0.16747	2.81	0.05191	1.56	160	2.7	157	4.1	119	52.2
2	90	468	2369	0.20	0.03410	1.60	0.23934	1.64	0.05109	0.32	216	3.4	218	3.2	237	7.6
3	61	256	1492	0.17	0.03730	1.63	0.25866	1.74	0.05196	0.38	236	3.8	234	3.6	208	13.5
4	34	867	1066	0.81	0.02436	1.64	0.16537	1.76	0.05039	0.59	155	2.5	155	2.5	159	15.0
5	39	1168	1117	1.05	0.02535	1.55	0.17533	3.34	0.06320	1.50	161	2.5	164	5.1	202	67.2
6	37	199	987	0.20	0.03404	1.67	0.23993	1.78	0.05198	0.55	216	3.5	218	3.5	246	14.2
7	47	159	1181	0.13	0.03600	2.81	0.25370	2.94	0.05161	0.83	228	6.3	230	6.1	246	20.0
8	58	304	1428	0.21	0.03614	1.72	0.25090	1.77	0.05035	0.41	229	3.9	227	3.6	211	9.6
9	17	385	526	0.73	0.02527	1.52	0.16674	1.97	0.05049	0.85	161	2.4	157	2.9	92	29.3
10	35	157	859	0.18	0.03723	2.00	0.26172	2.09	0.05099	0.62	236	4.6	236	4.4	240	14.1
11	12	223	384	0.58	0.02545	1.53	0.16718	2.26	0.05009	1.30	162	2.4	157	3.3	82	39.2
12	48	70	1194	0.06	0.03788	1.50	0.26623	1.56	0.05097	0.44	240	3.5	240	3.3	240	10.1
13	57	246	1362	0.18	0.03752	1.55	0.26354	1.61	0.05126	0.40	237	3.6	238	3.4	238	10.1
14	29	228	678	0.34	0.03749	1.53	0.26190	1.66	0.05147	0.57	237	3.6	236	3.5	226	14.9
15	27	84	675	0.13	0.03690	1.55	0.26172	1.78	0.05177	0.85	234	3.6	236	3.8	260	20.0
16	22	91	552	0.17	0.03584	2.65	0.25147	2.76	0.05202	0.66	227	5.9	228	5.7	236	18.0
17	15	278	500	0.56	0.02452	1.64	0.16469	2.24	0.05402	0.86	156	2.5	155	3.2	134	35.6
18	35	771	1101	0.70	0.02482	1.50	0.17071	2.16	0.05622	0.90	158	2.3	160	3.2	189	35.9
19	18	365	630	0.58	0.02332	2.20	0.16130	2.80	0.05587	1.17	149	3.2	152	4.0	203	39.5

Zircon DZ18-1, Zk003-104.5, BD-10, BD-23 and CH-CM-2 U–Pb dating use the LA-ICP-MS method, while the zircon CHBL-1 uses SIMS method

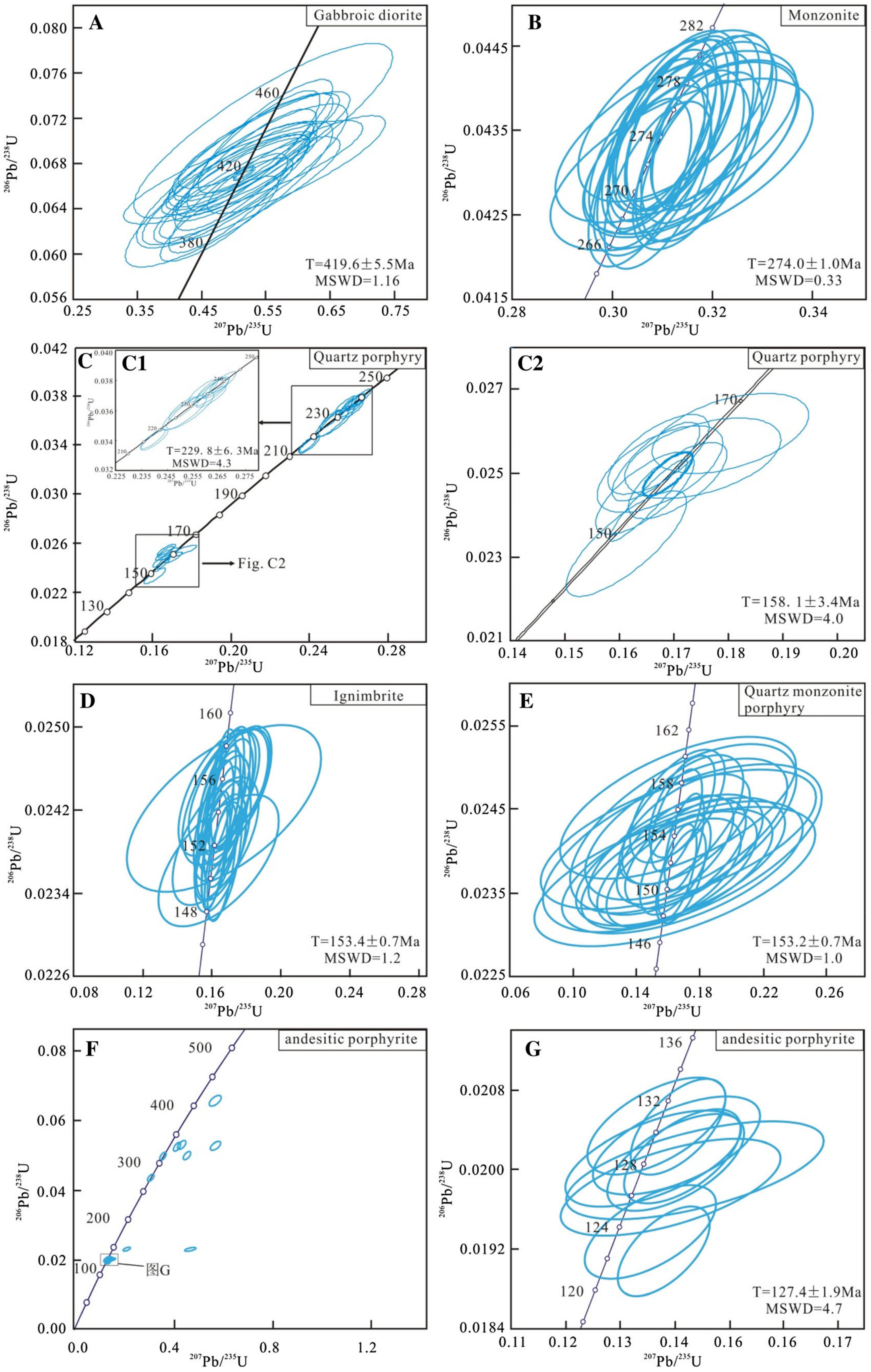

Fig. 4 Zircon U–Pb concordia diagrams for magmas in the Dongzi–Changhanboluo ore district

Table 2 Whole-rock chemical analyses for the magmatic rocks in Dongzi–Changhanboluo ore district

Sample	DZ18-1	DZ18-2	DZ18-3	CH-1	CH-2	CH-3	CH-4	CH-5	CH-6	CH-7	CH-8	CH-9	CH-K-3	CH-K-6
Rock type	DZ gabbroic diorite			CH monzonite					CH quartz porphyry					
SiO_2	52.88	50.77	51.32	59.72	59.87	57.98	57.68	58.14	78.66	78.76	75.76	76.07	76.75	75.81
Al_2O_3	19.96	19.72	20.14	16.35	16.15	16.93	16.64	16.72	13.26	11.89	12.81	12.47	13.16	12.81
Fe_2O_3	3.37	3.75	3.83	2.68	2.47	2.47	2.72	2.60	0.65	0.66	0.42	0.43	0.45	0.60
FeO	4.18	4.82	4.60	3.73	3.83	4.27	4.20	4.42	0.35	0.32	0.44	0.36	0.42	0.22
CaO	7.27	8.10	7.83	4.02	4.25	4.39	4.31	4.96	0.16	0.21	0.71	0.91	0.84	0.55
MgO	3.68	4.00	4.14	2.52	2.40	2.81	2.65	2.97	0.23	0.13	0.11	0.12	0.12	0.09
K_2O	1.01	1.11	0.79	3.85	3.85	3.47	3.36	3.19	3.91	5.90	4.86	5.05	5.35	6.03
Na_2O	3.92	3.63	3.82	3.88	3.91	4.12	3.71	3.64	0.10	0.17	2.64	2.33	0.20	1.56
TiO_2	0.73	0.85	0.85	0.99	1.01	1.02	0.98	1.00	0.05	0.05	0.06	0.06	0.06	0.06
P_2O_5	0.30	0.33	0.33	0.32	0.31	0.35	0.32	0.33	0.01	0.01	0.01	0.01	0.01	0.01
MnO	0.18	0.24	0.23	0.11	0.12	0.12	0.17	0.14	0.18	0.18	0.43	0.45	0.20	0.34
LOI	1.73	2.23	1.96	1.18	1.16	1.39	2.60	1.20	2.21	1.49	1.46	1.55	2.20	1.72
Total	99.19	99.56	99.83	99.35	99.33	99.32	99.34	99.31	99.77	99.77	99.71	99.81	99.76	99.80
La	30.43	28.78	28.94	45.40	45.90	41.00	42.30	36.40	10.90	12.20	9.11	11.40	13.00	6.55
Ce	57.54	57.38	56.50	84.50	84.90	72.40	76.70	64.00	28.90	32.70	31.30	32.80	34.70	30.40
Pr	6.34	6.52	6.20	11.60	11.60	10.50	10.60	9.45	3.80	4.13	3.10	3.62	4.32	2.14
Nd	24.06	25.31	23.69	44.80	45.00	41.60	41.30	37.80	15.50	16.60	12.40	14.60	17.60	8.79
Sm	4.18	4.37	4.07	8.64	8.60	7.95	7.93	7.44	5.08	5.11	3.96	4.51	5.68	2.65
Eu	1.33	1.43	1.48	1.88	1.93	1.86	1.87	2.00	0.14	0.09	0.07	0.07	0.10	0.04
Gd	3.42	3.69	3.39	7.62	7.59	7.02	6.94	6.35	5.65	5.15	3.99	4.44	5.94	2.79
Tb	0.52	0.55	0.50	1.14	1.15	1.09	1.04	0.98	1.18	1.00	0.86	0.93	1.26	0.57
Dy	2.83	3.17	2.76	6.28	6.32	5.77	5.81	5.37	7.66	6.27	5.36	5.87	8.08	3.53
Ho	0.57	0.61	0.54	1.21	1.17	1.09	1.08	1.00	1.48	1.17	1.05	1.14	1.53	0.66
Er	1.61	1.68	1.51	3.31	3.34	3.04	3.00	2.74	4.02	3.11	2.96	3.23	4.36	1.85
Tm	0.23	0.24	0.21	0.51	0.48	0.46	0.46	0.40	0.63	0.45	0.48	0.51	0.68	0.28
Yb	1.50	1.54	1.35	3.33	3.25	3.14	2.97	2.62	3.90	2.86	3.18	3.44	4.58	1.93
Lu	0.21	0.24	0.20	0.51	0.50	0.48	0.46	0.40	0.56	0.41	0.47	0.51	0.68	0.29
REE	134.78	135.52	131.34	220.73	221.73	197.40	202.46	176.95	89.40	91.25	78.29	87.07	102.51	62.47
Sr	857	807	860	544	544	703	542	697	24.7	34.6	34.4	34.4	52.8	46.5
Rb	40.88	41.91	35.49	98.70	111	75.40	91.80	81.50	187	228	180	183	226	233
Ba	340	385	288	960	1030	978	902	938	27.6	182	111	119	121	124
Th	1.87	1.52	1.50	10.30	12.30	7.27	9.54	8.88	22.30	20.90	17.90	19.40	22.80	12.60
Nb	5.15	5.52	5.21	11.30	11.30	10.10	9.26	7.76	25.40	29.00	34.30	32.20	33.20	33.00
Zr	156.1	92.4	100.9	320	291	259	348	170	90.8	79.1	74.9	84.1	80.8	81.7
Cs	12.92	9.61	11.42	4.96	2.77	3.28	6.06	3.28	11.20	8.83	3.67	3.88	11.00	6.33
Ga	23.03	23.48	23.70	19.40	19.20	19.60	19.70	19.00	17.50	14.40	14.70	14.70	15.60	14.40
Hf	3.50	2.27	2.38	8.59	7.98	6.70	9.14	5.04	5.77	4.84	4.85	5.22	5.36	5.13
Cr	7.82	8.79	8.26	7.61	11.80	9.75	13.90	12.40	1.27	3.93	4.13	2.35	1.04	2.37
V	136.11	154.74	153.78	126.00	124.00	135.00	148.00	150.00	1.99	0.46	1.54	0.55	1.71	2.41
Ni	6.57	7.78	7.95	10.80	12.20	10.60	12.70	12.60	0.58	1.99	1.60	0.82	1.13	0.77
Co	17.70	20.24	20.84	17.10	16.30	17.30	19.30	19.60	0.27	0.63	0.17	0.13	0.66	0.13
U	0.29	0.22	0.24	1.79	1.74	1.37	2.35	2.09	8.55	6.22	4.64	8.01	8.08	8.74
Y	15.86	17.21	15.34	29.70	29.30	27.30	27.10	24.00	35.30	28.30	25.80	27.20	37.40	15.50
Ta	0.23	0.24	0.22	0.66	0.67	0.53	0.57	0.50	2.52	2.45	2.67	2.70	2.68	2.57
Pb	5.21	5.62	5.66	18.50	19.00	15.00	14.90	16.60	80.30	363.00	366.00	545.00	23.00	77.70
Zn	125.40	187.17	111.87	99.00	78.00	74.50	66.80	74.40	51.90	177.00	345.00	262.00	42.40	67.20

Table 2 continued

Sample	BD-10	BD-26	BD-16	BD-17	BD-22	BD-23	BD-24	CH-CM-1	CH-CM-3	CH-CM-4
Rock type	CH ignimbrite	CH breccia tuff	CH quartz monzonite porphyry					CH andesite porphyry		
SiO_2	77.32	78.87	69.04	68.14	67.07	67.57	67.34	56.87	58.96	56.25
Al_2O_3	12.32	11.15	16.15	16.40	16.35	16.09	16.32	16.46	17.53	16.59
Fe_2O_3	0.68	1.01	2.10	2.60	2.00	2.05	2.39	1.18	0.92	1.34
FeO	0.22	0.37	0.27	0.20	0.50	0.40	0.36	3.46	3.58	3.62
CaO	0.19	0.29	0.85	0.74	1.74	1.63	1.55	4.36	2.41	5.05
MgO	0.16	0.08	0.53	0.55	0.50	0.56	0.40	1.78	1.63	1.48
K_2O	4.60	4.30	3.82	4.07	3.66	3.69	3.72	4.70	5.21	4.17
Na_2O	3.54	2.88	5.58	5.29	4.75	5.39	4.70	0.09	0.13	0.08
TiO_2	0.16	0.17	0.46	0.50	0.50	0.49	0.52	0.61	0.64	0.61
P_2O_5	0.02	0.01	0.13	0.13	0.14	0.15	0.15	0.34	0.36	0.34
MnO	0.01	0.03	0.04	0.05	0.04	0.03	0.06	0.26	0.44	0.18
LOI	0.52	0.65	0.82	1.07	2.52	1.75	2.26	9.26	7.64	9.68
Total	99.75	99.81	99.79	99.74	99.77	99.80	99.77	99.37	99.45	99.39
La	24.10	20.20	25.80	29.20	25.20	25.50	36.40	33.40	34.60	32.80
Ce	57.60	58.30	43.20	37.70	41.10	39.20	60.40	62.90	66.90	59.90
Pr	5.64	5.54	4.89	5.38	4.79	4.93	6.80	7.61	7.91	7.64
Nd	19.40	20.10	17.00	19.00	17.20	17.50	24.00	28.30	30.00	29.00
Sm	3.52	4.64	2.53	2.82	2.73	2.76	3.66	4.90	5.37	5.19
Eu	0.26	0.18	1.08	1.25	1.12	1.22	1.53	1.36	1.43	1.40
Gd	2.94	4.13	2.22	2.56	2.28	2.42	3.08	4.27	4.76	4.77
Tb	0.43	0.79	0.30	0.35	0.31	0.33	0.41	0.63	0.71	0.69
Dy	2.35	4.52	1.58	1.86	1.63	1.83	2.10	3.53	3.95	3.83
Ho	0.42	0.86	0.30	0.35	0.30	0.35	0.40	0.65	0.74	0.74
Er	1.08	2.31	0.86	1.02	0.90	1.00	1.12	1.86	2.07	2.05
Tm	0.16	0.34	0.14	0.15	0.15	0.17	0.18	0.28	0.32	0.31
Yb	0.98	2.19	0.99	1.04	0.94	1.10	1.21	1.83	2.09	2.04
Lu	0.14	0.31	0.16	0.17	0.16	0.19	0.19	0.30	0.34	0.32
REE	119.02	124.41	101.05	102.85	98.81	98.50	141.48	151.82	161.19	150.68
Sr	101	16.8	233	243	205	246	116	258	142	278
Rb	56.1	147.0	71.8	83.4	74.5	68.3	72.3	182.0	182.0	155.0
Ba	664	57.1	2330	2560	2160	2830	2880	432	197	640
Th	6.35	15.10	5.28	4.64	4.62	5.46	6.76	5.86	6.19	5.85
Nb	9.80	32.00	6.81	6.58	6.37	6.66	6.64	17.10	9.56	10.20
Zr	169	254	278	299	293	293	302	179	168	166
Cs	4.25	2.17	1.95	3.10	5.45	2.82	5.60	22.20	22.10	24.30
Ga	12.30	16.20	18.00	16.90	18.00	17.40	18.70	18.80	20.40	18.80
Hf	5.17	9.61	6.70	6.99	7.09	6.72	7.41	4.87	4.39	4.24
Cr	1.73	2.58	4.05	5.16	4.58	4.84	5.36	7.76	3.62	3.65
V	2.55	2.52	26.40	26.50	29.80	28.20	33.10	74.50	84.70	85.10
Ni	1.03	0.71	3.90	6.26	2.67	3.29	3.06	3.23	1.73	1.93
Co	0.36	0.23	2.62	2.42	3.25	2.91	3.82	9.48	8.05	9.69
U	1.70	3.80	1.16	0.88	0.82	0.86	1.40	1.65	1.89	3.09
Y	12.40	17.90	7.49	9.77	8.19	9.22	9.99	16.90	19.10	18.20
Ta	0.68	2.25	0.51	0.49	0.47	0.49	0.49	0.58	0.60	0.58
Pb	13.10	22.40	17.90	16.00	17.60	14.80	19.20	13.20	10.60	22.20

Table 2 continued

Sample Rock type	BD-10 CH ignimbrite	BD-26 CH breccia tuff	BD-16 CH quartz monzonite porphyry	BD-17	BD-22	BD-23	BD-24	CH-CM-1 CH andesite porphyry	CH-CM-3	CH-CM-4
Zn	34.80	56.30	46.70	44.60	55.00	43.40	59.50	73.50	138.00	82.00

Gabbroic diorite samples DZ18-1, DZ18-2 and DZ18-3 were taken from ore heaps of Dongzi deposit; Monzonite samples CH-1, CH-2, CH-3, CH-4 and CH-5 were taken from boreholes of ZK003-18.5 m, ZK003-45.5 m, ZK003-104.5 m, ZK806-312 m and ZK2005-530.2 m, respectively, from the Changhanboluo deposit; Quartz porphyry samples CH-6, CH-7, CH-8, CH-9 were taken from boreholes of ZK004-293.5 m, ZK004-302.5 m, ZK004-415.2 m and ZK004-418.6 m, respectively, and CH-K-3, CH-K-6 were taken from the Changhanboluo deposit; Ignimbrite sample BD-10, breccia tuff sample BD-26 and quartz monzonite porphyry samples BD-16, BD-17, BD-22 BD-23 BD-24 were taken from the north part of the Changhanboluo deposit; Andesitic porphyrite samples CH-CM-1, CH-CM-3 and CH-CM-4 were taken from the Changhanboluo deposit

[$Mg^{\#} = 100\ Mg/(Mg + TFe^{2+})$] = 47–48, and $Na_2O + K_2O$ = 4.61–4.93 wt% (Table 1), and they belong to the subalkaline (Fig. 5a) and calc-alkaline series (Fig. 5b).

The gabbroic diorites have 131.34–135.52 ppm of total REEs and display coherent REE patterns characterized by relatively light rare earth element (LREE) enrichment and heavy rare earth element (HREE) depletion ($(La/Yb)_N$ = 12.58–14.46), with weak positive Eu anomalies (δEu = 1.05–1.19) (Fig. 6a). They are enriched in large ion lithophile elements (LILEs), such as Rb, Ba, K, and LREEs, but depleted in high-field strength elements (HFSEs), such as Nb, Ta, Ti, and HREEs (Fig. 6b).

5.2.2 *Middle Permian magmas*

The Middle Permian magmas are the Herwusu monzonites in the study area. The monzonites have compositional ranges of 57.68–59.87 wt% SiO_2 and 16.15–16.93 wt% Al_2O_3. They are enriched in $Na_2O + K_2O$ (6.83–7.76 wt%), with Na_2O/K_2O ratios ranging from 1.01 to 1.19. All samples plot in the monzonite field on the total alkali-silica (TAS) diagram (Fig. 5a) and the high-K calc-alkaline to shoshonitic series area on the SiO_2 versus K_2O diagram (Fig. 5b).

The monzonites are enriched in LREEs but depleted in HREEs (Fig. 6a), with total REEs of 176.95–221.73 ppm and slightly negative Eu anomalies (δEu: 0.69–0.87). All samples are enriched in LILEs, such as Rb, Ba, Th, U, K, and LREEs, but have negative anomalies for HFSEs (e.g., Nb, Ta, P, Ti, and HREEs) compared to the primitive mantle (Fig. 6b). At the same time, the monzonites present high Sr contents (542–703 ppm, average 606 ppm) and Sr/Y values (18–29, average 22).

5.2.3 *Late Jurassic magmas*

The Late Jurassic magmas in the study area consist of a series of quartz porphyry, ignimbrite, breccia tuff, and quartz monzonite porphyry.

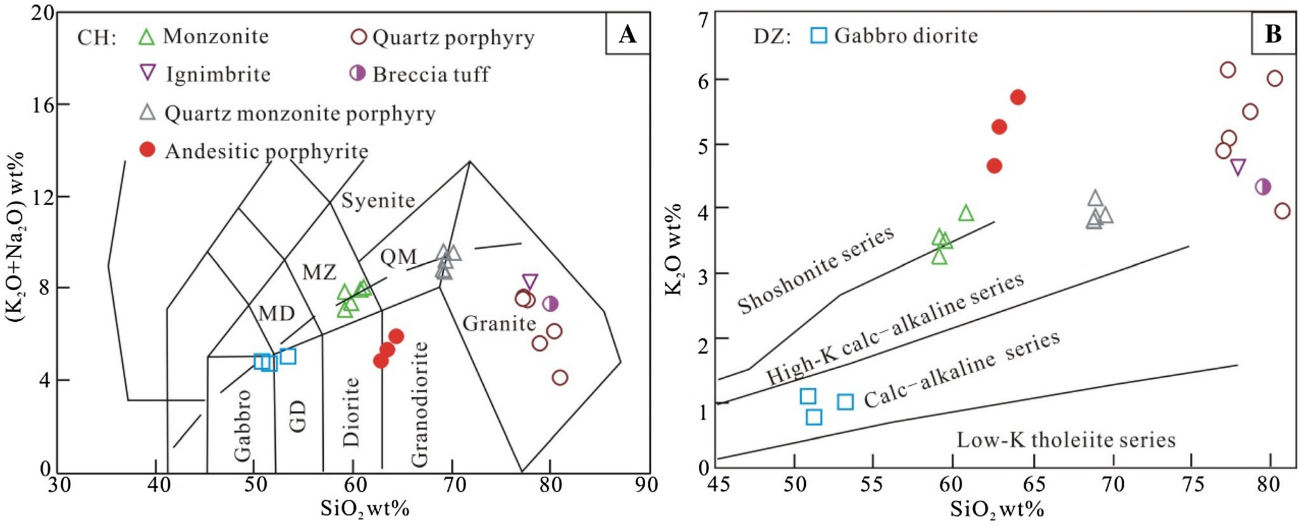

Fig. 5 SiO_2 versus total alkali ($Na_2O + K_2O$) (**a**) and SiO_2 versus K_2O (**b**) diagrams for the Early Paleozoic–Mesozoic magmas in the study area. The boundary lines in the SiO_2 versus ($Na_2O + K_2O$) and SiO_2 versus K_2O diagrams are from Irvine and Baragar (1971) and Peccerillo and Taylor (1976), respectively. Abbreviations: CH, Changhanboluo mining area; DZ, Dongzi mining area; GD, gabbroic diorite; MD, monzodiorite; MZ, monzonite; QM, quartz monzonite

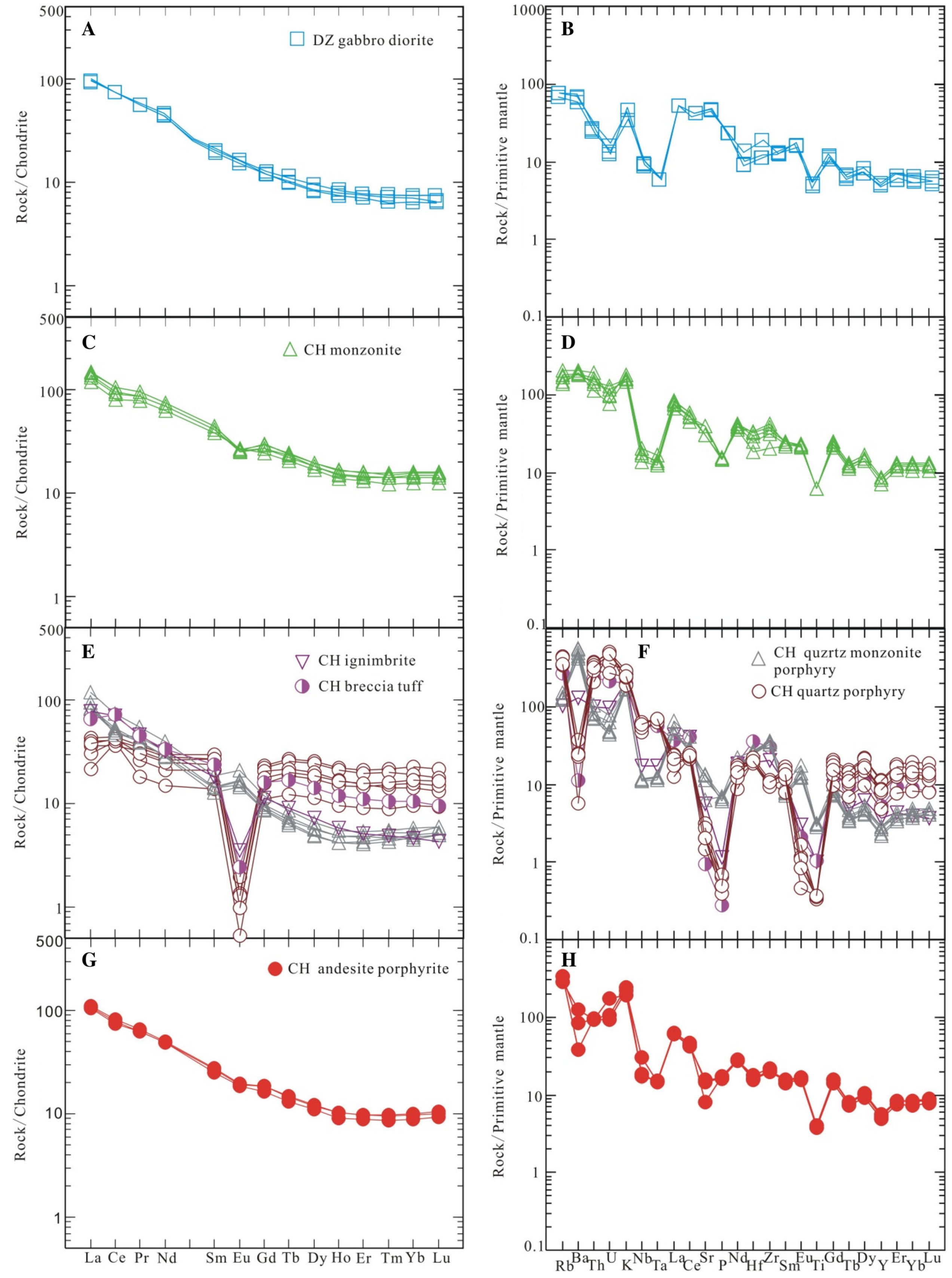
A
DZ gabbro diorite
Rock/Chondrite
500
100
10
1
B
Rock/Primitive mantle
1000
100
10
1
0.1
C
CH monzonite
D
E
CH ignimbrite
CH breccia tuff
F
CH quzrtz monzonite porphyry
CH quartz porphyry
G
CH andesite porphyrite
H
La Ce Pr Nd Sm Eu Gd Tb Dy Ho Er Tm Yb Lu
Rb Ba Th U K Nb Ta La Ce Sr P Nd Hf Zr Sm Eu Ti Gd Tb Dy Y Er Yb Lu

◀**Fig. 6** Chondrite-normalized REE patterns (**a**, **c**, **e**, **g**) and primitive mantle-normalized trace element spidergrams (**b**, **d**, **f**, **h**) for the Early Paleozoic–Mesozoic magmas in the study area. Chondrite and primitive mantle normalization values are from Boynton (1984) and McDonough et al. (1992), respectively. Abbreviations: CH, Changhanboluo mining area; DZ, Dongzi mining area

The quartz porphyries have high SiO_2 (75.76–78.76 wt%), K_2O (3.91–5.90 wt%) and MgO (11.89–13.26 wt%) contents and low CaO (0.16–0.91 wt%) and TiO_2 (0.051–0.057 wt%) contents. All the samples plot in the granite field on the TAS diagram (Fig. 5a) and the high-K calc-alkaline and shoshonite series on the SiO_2 versus K_2O diagram (Fig. 5B). These quartz porphyries have "Seagull"-type REE patterns, with very low ΣREE (78.29–102.51 ppm) and strongly negative Eu anomalies (δEu = 0.05–0.08) (Fig. 6e). Additionally, the rocks show high Rb (180–228 ppm), Ga (14.4–17.5 ppm), Zr (74.9–90.8 ppm), Nb (25.4–34.3 ppm), and Y (25.8–37.4 ppm) contents and low Sr (24.7–52.8 ppm), Ba (27.6–182 ppm), Cr (average 2.0 ppm), and Ni (average 1.5 ppm) contents and exhibit strongly negative Ba, Sr, P, and Ti anomalies on the spider diagram of trace elements (Fig. 6f).

The ignimbrite and breccia tuff in the western part of the Dongzi–Changhanboluo ore district have high SiO_2 (77.32 and 78.87 wt%) and low MgO (0.16 and 0.08 wt%) contents. Their A/CNK [molar $Al_2O_3/(CaO + K_2O + Na_2O)$] values are 1.11 and 1.12, respectively, which are indicative of peraluminous granites (Maniar and Piccoli 1989). All the samples plot in the granite field on the TAS diagram (Fig. 5a) and the high-K calc-alkaline series on the SiO_2 versus K_2O diagram (Fig. 5b). The ignimbrite and breccia tuff have lower REEs (119.02 and 124.41 ppm), Yb (0.98 and 2.19 ppm) and δEu (0.24, 0.12). In addition, the ignimbrite and breccia tuff show similar trace element partition models, except for strongly negative Ba, Sr, P, and Ti anomalies. Overall, the REE and trace element distribution patterns of ignimbrite and breccia tuff are similar to those of quartz porphyry (Fig. 6e, f).

The quartz monzonite porphyry has SiO_2 = 67.07–69.04 wt%, TiO_2 = 0.46–0.52 wt%, and Al_2O_3 = 16.09–16.35 wt% and belongs to the high-K calc-alkaline series (Fig. 5b). The samples have total REE contents (ΣREE) ranging from 98.50 to 141.48 ppm and show distinct REE enrichment [$(La/Yb)_N$ = 15.63–20.28] and positive Eu anomalies (δEu = 1.34–1.41) on chondrite-normalized REE diagrams (Fig. 6e). On primitive mantle-normalized spidergrams, the samples exhibit similar trace element patterns, with depletions in Nb, Ta, P, and Ti and enrichments in Ba and Eu (Fig. 6f).

5.2.4 *Early Cretaceous magmas*

The Early Cretaceous magmas formed an andesitic porphyrite that cuts through the ore veins in the Changhanboluo deposit and underwent obvious carbonation alteration. The andesite porphyrite has SiO_2 = 56.25–58.96 wt% and Al_2O_3 = 16.46–17.53 wt%. The samples have lower ΣREE (150.68–161.19 ppm) and weak negative Eu anomalies (δEu = 0.85–0.89) on the chondrite-normalized REE diagram (Fig. 6g). On the primitive mantle-normalized spidergram, the samples exhibit enrichments in LILEs but depletions in HFSEs, with weak depletions in Nb, Ta, Sr, and Ti (Fig. 6h).

5.3 Sr–Nd isotopes

The whole-rock Sr–Nd isotope data are listed in Table 3 and plotted in Fig. 7. The initial $^{87}Sr/^{86}Sr$ ratios and the $\varepsilon_{Nd}(t)$ values are calculated according to their zircon U–Pb ages.

The Late Silurian Dongzi gabbroic diorites show homogeneous Sr–Nd isotope compositions characterized by $(^{87}Sr/^{86}Sr)_i$ = 0.706338–0.706347 and $\varepsilon_{Nd}(t)$ values from − 15.22 to − 14.78. The Middle Permian Herwusu monzonites have $(^{87}Sr/^{86}Sr)_i$ ratios of 0.704974 to 0.705002 and $\varepsilon_{Nd}(t)$ values of − 8.18 to − 7.47. The Late Jurassic magmas of quartz porphyry and quartz monzonite porphyry show similar Sr–Nd isotope data characterized by $(^{87}Sr/^{86}Sr)_i$ = (0.705422–0.707590) and $\varepsilon_{Nd}(t)$ values from − 8.36 to − 6.89. The Early Cretaceous andesitic porphyrites are similar to the Late Jurassic magmas, with $(^{87}Sr/^{86}Sr)_i$ = 0.706133–0.706225 and $\varepsilon_{Nd}(t)$ values from − 9.29 to − 8.89.

6 Discussion

6.1 Petrogenesis

6.1.1 *Late Silurian magmas*

The Late Silurian gabbroic diorites have low SiO_2 contents (50.77–52.88 wt%) and high $Mg^{\#}$ (47–48), CaO (7.27–8.10 wt%), and Na (Na_2O/K_2O = 3.28–4.82) contents, which indicate the partial melting of ultramafic rocks from the mantle. The mantle is usually divided into the asthenospheric mantle and lithospheric mantle. Different mantle sources show different geochemical properties. The ratios of LILEs to HFSEs can trace the sources of magmas. For example, $La/Nb < 1.5$ and $La/Ta < 22$ imply asthenospheric mantle, while $La/Nb > 1.5$ and $La/Ta > 30$ indicate lithospheric mantle (Fitton et al. 1988; Leat et al. 1988). The gabbroic diorite displays obviously higher La/

Table 3 Sr–Nd isotope compositions for the magmatic rocks in Dongzi–Changhanboluo ore district

Sample	T/Ma	Rb/ ppm	Sr/ ppm	^{87}Rb/ ^{86}Sr	^{87}Sr/ ^{86}Sr	2 s	(^{87}Sr/ ^{86}Sr)i	Sm/ ppm	Nd/ ppm	Sm/ Nd	^{143}Nd/ ^{144}Nd	2 s	(143Nd/ 144Nd)i	ε_{Nd}
DZ18-1	419.6	40.9	857.0	0.1382	0.707164	9	0.706338	4.18	24.06	0.1051	0.511607	12	0.511318	− 15.22
DZ18-3	419.6	35.5	860.0	0.1195	0.707061	7	0.706347	4.07	23.69	0.1039	0.511626	13	0.511340	− 14.78
CH-1	274	98.70	544.0	0.5253	0.707022	9	0.704974	8.64	44.80	0.1167	0.512112	7	0.511903	− 7.47
CH-2	274	111.1	599.0	0.5369	0.707095	13	0.705002	7.68	40.24	0.1156	0.512074	8	0.511866	− 8.18
CH-3	274	85.95	830.6	0.2995	0.706162	12	0.704995	7.13	37.02	0.1165	0.512087	8	0.511878	− 7.96
CH-7	158.1	228.0	34.60	19.0802	0.750473	15	0.707590	5.11	16.60	0.1862	0.512258	8	0.512065	− 7.20
CH-8	158.1	221.7	39.40	16.34	0.742153	16	0.705422	6.45	19.26	0.2025	0.512233	8	0.512023	− 8.03
CH-K-6	158.1	233.0	46.50	14.5086	0.739432	10	0.706823	2.65	8.79	0.1824	0.512270	5	0.512081	− 6.89
BD-10	153.4	56.10	101.0	1.6083	0.737286	13	0.733779	3.52	19.40	0.1098	0.512210	12	0.512100	− 6.65
BD-17	153.2	85.06	275.3	0.8943	0.707803	12	0.705858	4.02	26.21	0.0929	0.512122	10	0.512029	− 8.03
BD-22	153.2	89.66	255.4	1.016	0.707840	13	0.705630	3.59	23.39	0.0929	0.512106	10	0.512013	− 8.35
BD-23	153.2	82.13	307.8	0.7724	0.707486	14	0.705806	3.81	25.32	0.0912	0.512104	8	0.512013	− 8.36
CH-CM-1	127.4	182.0	258.0	2.0426	0.709924	10	0.706225	4.90	28.30	0.1048	0.512106	14	0.512019	− 8.89
CH-CM-3	127.4	182.0	142.0	3.7111	0.712853	7	0.706133	5.37	30.00	0.1083	0.512088	5	0.511998	− 9.29

Chondrite Uniform Reservoir (CHUR) values (^{87}Rb/^{86}Sr = 0.0847, ^{87}Sr/^{86}Sr = 0.7045, ^{147}Sm/^{144}Nd = 0.1967, ^{143}Nd/^{144}Nd = 0.512638) are used for the calculation. $\lambda_{Rb} = 1.42 \times 10^{-11}$ year^{-1}(Steiger and Jäger 1977); $\lambda_{Sm} = 6.54 \times 10^{-12}$ year^{-1} (Lugmair and Marti 1978)

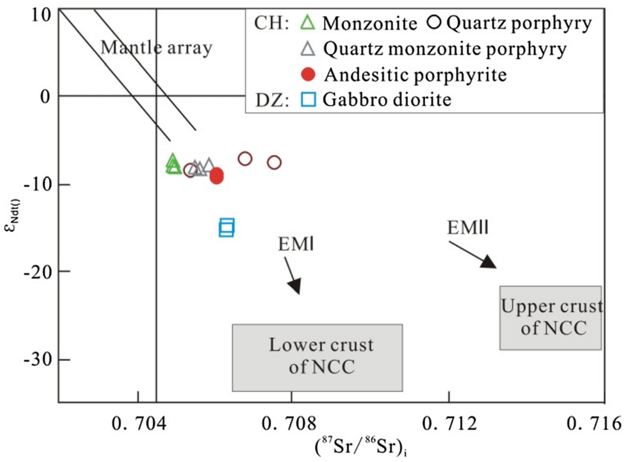

Fig. 7 (^{87}Sr/^{86}Sr)$_i$ versus ε_{Nd}(t) diagram for magmas in the Dongzi–Changhanboluo ore district. The Sr–Nd isotope data of the lower and upper crust are derived from Jahn et al. (1999)

Nb (5.21–5.91) and La/Ta (120.2–133.6) than the values of the asthenospheric mantle. Together with the enrichment in LILEs and depletion of HFSEs and HREEs, these data suggest that the source of the gabbroic diorites was not the asthenospheric mantle but the enriched continental lithospheric mantle (Song et al. 2015).

Compared with the major and trace element compositions of the intrusion, the radiogenic isotope ratios, which are less affected by magma evolution processes such as fractional crystallization, can be more useful for interpreting magma sources (e.g., Li et al. 2014, 2015). The gabbroic diorites have relatively homogeneous ε_{Nd}(t) values from − 15.22 to − 14.78 and (^{87}Sr/^{86}Sr)$_i$ ratios between 0.706338 and 0.706347. In the (^{87}Sr/^{86}Sr)$_i$–ε_{Nd}(t) diagram, all the samples plot near the enriched mantle 1 (EM1) field. Therefore, we conclude that the gabbroic diorite may have been sourced from EM1-type mantle.

6.1.2 Middle Permian magmas

The Middle Permian magmatic rocks are the Herwusu monzonite batholiths in the study area. The rocks are characterized by high alkali contents ($K_2O + Na_2O > 5$ wt%) and K_2O/Na_2O values ($K_2O/Na_2O > 0.5$ and 1.0 when $SiO_2 = 50$ and 55 wt%, respectively) and low TiO_2 contents (mostly < 1.3 wt%). The contents of Al_2O_3 are higher and have a large range of variability (mostly between 14 and 19 wt%). The rocks show strong enrichment in LILEs (such as average values of Rb = 91.7, Ba = 962, and Sr = 606, in ppm) and LREEs, which are characteristics of the shoshonitic rock series (Morrison 1980). In Fig. 8, the samples are all located in the shoshonitic series area. The shoshonitic series was limited to volcanic rocks in the past (Morrison 1980). Current studies show that the potassium basalt series is not confined to volcanic rocks but also includes intrusive rocks (Fowler and Henney 1996; Eklund et al. 1998). Therefore, the monzonite in this area belongs to the shoshonitic series.

The shoshonitic rocks mainly originated from the metasomatic mantle enriched in potassium and LILEs, which are associated with subduction (Foley and Peccerillo 1992). Such rocks are mostly formed in island arc or continental arc settings but can also occur in intraplate and post-collision settings (Muller and Groves 1995; Deng

Table 4 Lead isotopic analyses for the magmatic rocks and ores in Dongzi–Changhanboluo ore district

Magma/deposit	Sample	Rock/mineral	$(^{206}Pb/^{204}Pb)_i$	$(^{207}Pb/^{204}Pb)_i$	$(^{208}Pb/^{204}Pb)_i$
Magma	DZ18-1	Gabbroic diorite	16.163	15.382	36.817
	DZ18-3	Gabbroic diorite	16.128	15.380	36.763
	CH-1	Monzonite	16.914	15.351	36.923
	CH-2	Monzonite	16.920	15.368	36.923
	CH-3	Monzonite	16.829	15.333	36.830
	CH-7	Quartz porphyry	17.312	15.434	37.648
	CH-8	Quartz porphyry	17.084	15.375	37.358
	CH-K-6	Quartz porphyry	17.119	15.409	37.570
	BD-10	Ignimbrite	17.412	15.456	37.774
	BD-17	Quartz monzonite porphyry	17.474	15.428	37.705
	BD-22	Quartz monzonite porphyry	17.453	15.429	37.713
	BD-23	Quartz monzonite porphyry	17.483	15.464	37.816
	CH-CM-1	Andesitic porphyrite	17.306	15.420	37.596
	CH-CM-3	Andesitic porphyrite	17.225	15.397	37.443
Changhanboluo deposit	ZK003-265	Pyrite	17.23	15.449	37.695
	ZK003-265	Galena	17.202	15.402	37.536
	CH-K-19	Galena	17.181	15.384	37.48
	CH-K-7	Galena	17.200	15.405	37.563
	CH-K-7	Sphalerite	17.374	15.416	37.823
Dongzi deposit	HGT-1	Chalcopyrite	17.25	15.452	37.697
	HGT-1	Sphalerite	17.254	15.447	37.689
	HGT-1	Galena	17.182	15.371	37.425
	HGT-2	Sphalerite	17.211	15.389	37.496
	HGT-11	Galena	17.243	15.458	37.703
	HGT-11	Sphalerite	17.212	15.403	37.527
	HGT-11	Chalcopyrite	17.264	15.476	37.768
	HGT-13	Sphalerite	17.255	15.467	37.74
	HGT-13	Galena	17.199	15.398	37.514

$(^{206}Pb/^{204}Pb)_i$, $(^{207}Pb/^{204}Pb)_i$ and $(^{208}Pb/^{204}Pb)_i$ present initial Pb isotopic ratios when the rock formed, calculated using single-stage model

et al. 2004; Li et al. 2006; Xia et al. 2006). The shoshonitic rocks associated with island arcs are highly enriched in LREEs and LILEs and significantly depleted in Nb, Ta and Ti (Li et al. 2001). The shoshonitic rocks in an oceanic plate have trace element characteristics of oceanic island basalts (OIB) (Weaver 1991), while those in a continental plate have both island arc and OIB trace element characteristics (Chung et al. 2001; Zou et al. 2003). The monzonites have LREEs and LILEs enrichments and Nb, Ta, and Ti depletions. These characteristics are all typical island arc magmatic characteristics, and in the $(La/Yb)_N$–Yb_N and Sr/Y–Y diagrams (Fig. 9), the samples all plot in the classic island arc field.

The monzonites also have homogeneous $\varepsilon_{Nd}(t)$ values from − 8.18 to − 7.47 and $(^{87}Sr/^{86}Sr)_i$ ratios from 0.704974 to 0.705002, which are higher $\varepsilon_{Nd}(t)$ and lower $(^{87}Sr/^{86}Sr)_i$ values than those of theLate Silurian gabbroic diorites. The Sr–Nd isotope compositions of the monzonites represent the slightly enriched mantle-derived material in this region. Because of the similar partition coefficients of Nb and U, the Nb/U ratio can reflect the characteristics of the source region (Chung et al. 2001). The Herwusu monzonites have Nb/U ratios (3.7–7.4, average 5.6) lower than those of mid-ocean ridge basalts (MORB) and OIB (average 50) and the silicate Earth (average 32) and slightly lower than that of the upper crust (average 9). In Fig. 10a, most of the samples plot in the arc volcanic rock field. The lower Nb/U ratios may indicate fluid metasomatism in the subduction zone. In addition, the Ce/Pb ratio of monzonite (3.86–5.15, average 4.57) is significantly lower than those of oceanic basalts (average 25) and the silicate Earth (average 11) and slightly higher than that of the upper crust (average 3.2). In Fig. 10b, the samples are located above the upper crust field, near the arc

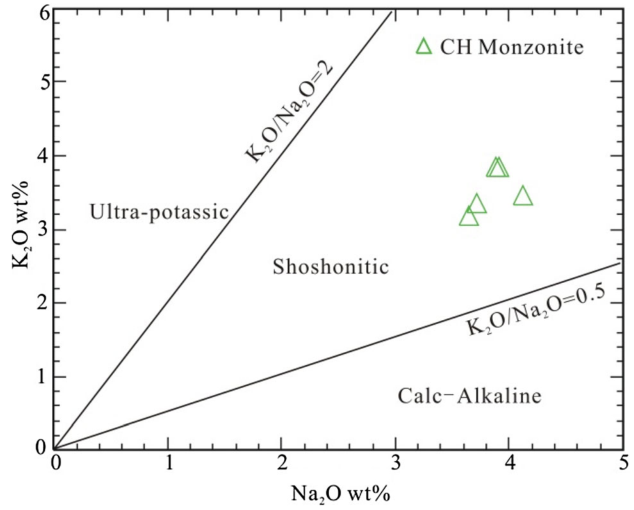

Fig. 8 K_2O versus Na_2O diagram for the Middle Permian Herwusu monzonite. (After Turner et al. 1996)

volcanic rock field. Therefore, the monzonite in this area is suggested to have originated mainly from the metasomatic mantle rich in potassium and LILEs related to subduction. Against the background of subduction, the source may have been the mantle zone of metasomatism, where fluid/melt was released by the subducting plate. The higher Al_2O_3 content (16.15–16.93 wt%), Th/Ce ratio (0.10–0.14) and Th/Nb ratio (0.72–1.14) and lower Pb/Nd ratio (0.36–0.44) and Ce/Pb ratio (3.86–5.15) all indicate the addition of subducted sediments in the mantle source area.

Al_2O_3 content is an important indicator of pressure. The pressure is less than 16 kbar when $Al_2O_3 < 15$ wt% and the residues are amphibole, plagioclase and orthopyroxene. The pressure is greater than 16 kbar when $Al_2O_3 > 15$ wt% and the residual phases are clinopyroxene, amphibole, plagioclase and garnet (Rapp et al. 1991). When the pressure is between 20 and 30 kbar, the melt equilibrates with garnet-bearing, plagioclase-free amphibolite-, granulite- or eclogite-facies rocks (Rapp et al. 1991; Rapp and Watson 1995). The content of Al_2O_3 in the monzonite (16.15–16.93 wt%) is greater than 15 wt%, which indicates that the formation pressure of the monzonite was > 16 kbar. The Sr/Y ratio is mainly controlled by the relative contents of garnet, amphibole and plagioclase in the residual phase. A high content of garnet and low contents of amphibole and plagioclase in the residual phase lead to a high Sr/Y ratio (Springer and Seck 1997). High Sr/Y ratios (average 22) in the monzonite may indicate the existence of garnet but not plagioclase in the residual phase, which is consistent with the weak Eu anomaly (Fig. 6c). Therefore, the monzonite may have been formed under moderate or high pressure, which is consistent with its high Sr and Yb characteristics (Zhang et al. 2006).

6.1.3 Late Jurassic magmas

The Late Jurassic magmatic rocks are widely distributed in this area, forming a large range of intermediate-acid volcaniclastic rocks and subvolcanic veins (including ignimbrite, breccia tuff, and quartz monzonite porphyry veins) in the western part of the study area and quartz porphyry in the Changhanboluo mining area.

Granitic rocks should originate mainly from the partial melting of crustal rocks, regardless of how strongly the geochemistry is imprinted by the mantle because the partial melting of mantle peridotite cannot directly produce granitic melts (Liu et al. 2002). The ignimbrite and breccia tuff have similar geochemical characteristics that may indicate the same magma source. They all have high SiO_2

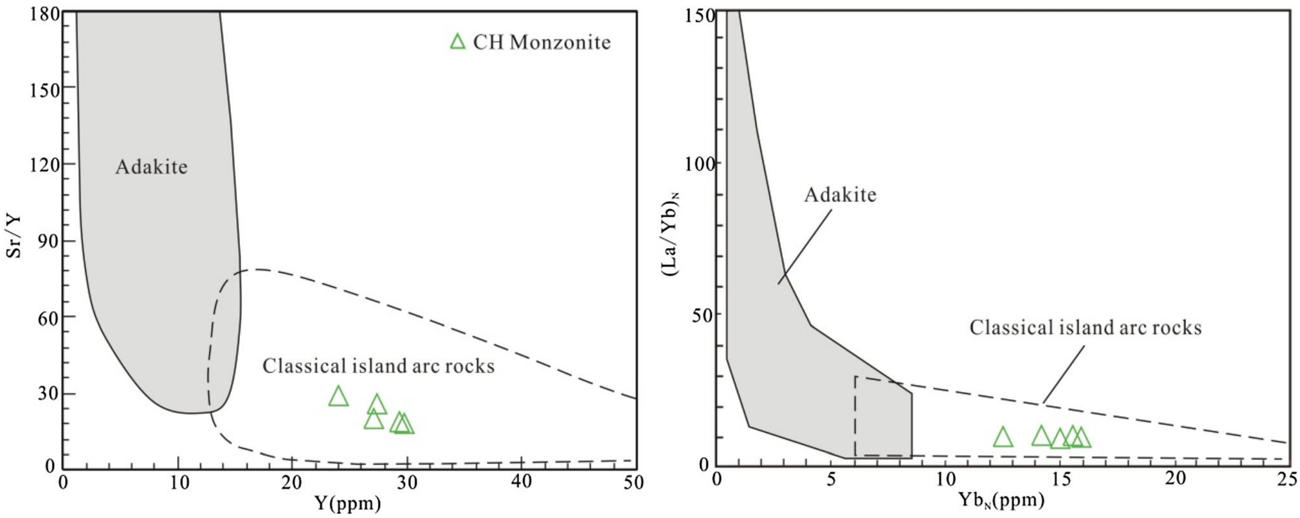

Fig. 9 Sr/Y–Y and $(La/Yb)_N$–Yb_N diagrams for the Middle Permian Herwusu monzonite. (After Defant and Drummond 1990 and Martin et al. 2005)

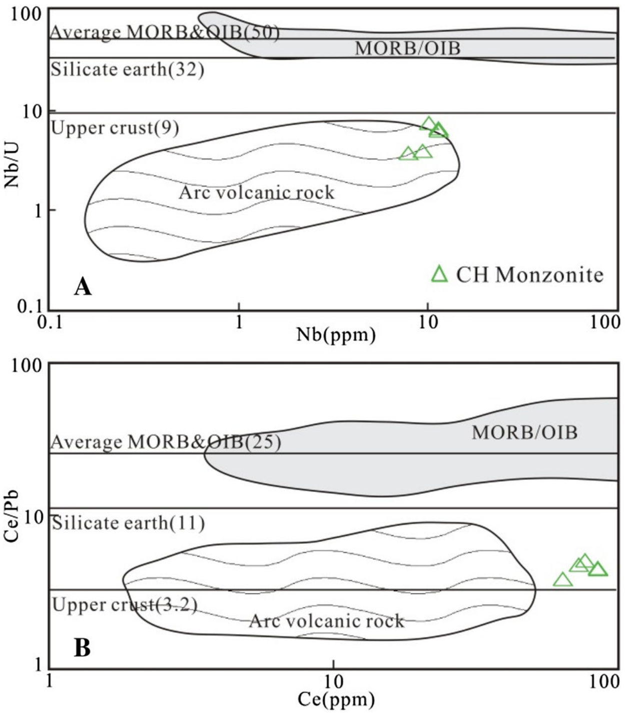

Fig. 10 Nb/U-Nb (**a**) and Ce/Pb–Ce (**b**) diagrams for the Middle Permian Herwusu monzonit. (After Chung et al. 2001)

contents, low CaO and MgO contents, and high aluminum saturation index (ASI) values (average 1.1), which mark peraluminous rocks. Corundum occurs as a CIPW normative mineral, and the content is more than 1%, which is consistent with the characteristics of typical S-type granite (ASI > 1.1 and the CIPW normative corundum content > 1%, Chappel and White 1974). The source area may have been argillaceous rock with low CaO/Na_2O ratios (average 0.08, < 0.3) (Sylvester 1998).

The Al_2O_3/TiO_2 ratio in peraluminous granite can be used as an indicator of the partial melting temperature of source rocks. Previous studies show that when the ratio of Al_2O_3/TiO_2 is less than 100, the partial melting temperature of the source region is greater than > 875 °C, while when the ratio of Al_2O_3/TiO_2 is greater than 100, the partial melting temperature of the source region is less than 875 °C; thus, the ratio of Al_2O_3/TiO_2 is inversely related to the formation temperature (Sylvester 1998). The ratios of Al_2O_3/TiO_2 of the volcanic clastic rocks in this area are between 66 and 77 (all less than 100), indicating that the partial melting temperature in the source may have been higher than 875 °C. By combining this information with the whole-rock saturation temperature of zirconium (840–879 °C), we can conclude that the volcaniclastic rocks are high-temperature peraluminous granites. The enrichments in LREEs and depletions in HREEs and Y(Yb) indicate the existence of garnet, while the strong depletion in Sr and Eu indicates the existence of plagioclase in the residual phase. Xiong et al. (2005) showed that when the melting pressure exceeds a certain range, the contents of some trace elements in the melt are changed, such as the pressure-sensitive elements Y and Yb (mainly related to garnet). Zhang et al. (2006) also noted that the formation pressure can be inferred from the composition of the residual phase and the contents of Sr and Yb in granite. The low Sr content (16.8–101, average 58.9 < 400, in ppm) and low Yb content (0.98–2.19, average 1.59 < 2, in ppm) of volcaniclastic rocks indicate that they were formed under moderate pressure (0.8–1.5 GPa), with garnet + plagioclase as the main residual phase, and the corresponding crustal thickness was approximately 40–50 km (Zhang et al. 2010c). Therefore, in this paper, we infer that the Jurassic volcaniclastic rocks are medium-pressure and high-temperature granites, which may have formed against the background of crustal thickening in a syncollisional stage or the early postcollisional stage. During this process, muddy sedimentary rocks were brought into the deep crust and heated (including radioactive decay and heat generation), followed by a rapid isostatic uplift of the crust, which caused the partial melting of the sedimentary rocks due to decompression.

In addition to volcaniclastic rocks, the Sr–Nd isotope compositions of the quartz monzonite porphyry and quartz porphyry are similar to those of Permian magmatic rocks [$\varepsilon_{Nd}(t) = -8.36$ to -6.65; $(^{87}Sr/^{86}Sr)_{i} = 0.705422–0.707590$], indicating source areas similar to those of the Late Permian monzonite. Quartz monzonite porphyry also has low Sr contents (116–246, average 209 < 400, in ppm) and low Yb contents (0.94–1.21, average 1.06 < 2, in ppm). The enrichment in LREEs and depletion in HREEs and Y(Yb) indicate the existence of garnet, while the depression between middle rare earth elements (MREEs) and HREEs in the REE distribution curve and $Ho_N < Yb_N$ (MREE depletion) suggests that hornblende may have been an important residual phase. The positive Eu and Ba anomalies may indicate that there was no residual plagioclase in the source area. Therefore, the quartz monzonite porphyry may have been formed by partial melting of the mantle metasomatized by subducted sediment, and the residual phases in the source area were mainly garnet and hornblende but not plagioclase.

The quartz porphyry is characterized by high silicon and alkalis, low calcium, magnesium and iron, and significant depletion of Ba, Sr, P, Ti, and Eu, which may indicate a high degree of differentiation and evolution. However, due to the similar characteristics of highly evolved I- and S-type granites (SiO_2 > 74 wt%) and A-type granites, accurately distinguishing their types by chemical composition is particularly important. Quartz porphyry has a relatively low FeO*/MgO ratio (4.06–7.44), despite its high alkali content, which is different from that of A-type granite (FeO*/MgO > 10, Whalen et al. 1987). The Ga content of quartz porphyry is relatively low, with a 10,000*Ga/Al ratio of 2.17–2.49 (average 2.28), which is lower than that of A-type granite (Whalen et al. 1987). The contents of Zr, Nb, Ce, and Y are relatively low, with the content of Zr + Nb + Ce + Y from 166 to 186 ppm, which is significantly lower than the lower limit for A-type granite (350 ppm) recommended by Whalen et al. (1987). In the discriminant diagrams based on Ga/Al proposed by Whalen et al. (1987) (Fig. 11a, b), all the samples plot in non-A-type granite fields. In the discriminant diagrams for A-type and differentiated granites, the samples are mainly located in highly differentiated granite fields (Fig. 11c, d). Experiments by Clemens et al. (1986) and Watson and Harrison (1983) show that the distribution coefficient of zirconium D^{Zr} zircon/melt is a function of the principal component parameter M = (Na + K + 2Ca)/(Si*Al) and the melt temperature. Given the M value and Zr content of the whole rock, the saturation temperature of zircon (close to the liquidus temperature) can be calculated, indicating the minimum initial temperature of magma in the source area. The saturation temperature of quartz porphyry is 757–818 °C, with an average of 780 °C, which is lower than the average value of 839 °C (n = 55) for aluminous A-type granite in the Lachlan fold belt, Australia (King et al. 1997). Therefore, in this paper, we consider that the quartz porphyry is not an A-type granite but a highly differentiated granite. The significant depletions in Sr and Eu are due to the crystallization of plagioclase. The obvious Ba anomaly is more closely related to the crystallization of potassium feldspar (Han et al. 1997). The obvious P depletion may be caused by apatite separation and crystallization, while the Ti depletion may be caused by ilmenite, titanite and rutile separation, and crystallization, but rutile has a high distribution coefficient for Nb and Ta, and its separation and crystallization can also result in Nb and Ta depletion. However, the Nb and Ta depletions are not obvious on the trace element spidergrams, so the Ti depletion may have been caused by the separation and crystallization of ilmenite and rutile.

Therefore, in this paper, we infer that the quartz monzonite porphyry and quartz porphyry were formed by partial melting of a mantle source area metasomatized by subducted sediments, but the quartz porphyry experienced a high degree of differentiation and evolution. The Jurassic volcaniclastic rocks were formed in a medium-pressure and high-temperature environment, possibly against the background of crustal thickening in a syn-collisional stage and the early postcollisional stage. During this process, muddy sedimentary rocks were brought into the deep crust and heated, followed by the rapid isostatic uplift of the crust, which caused partial melting of the sedimentary rocks.

6.1.4 *Early Cretaceous magmas*

Cretaceous magmatism is mainly manifested by the latest andesitic porphyrite dike intruded in quartz porphyry. The andesitic porphyrite shows a serious carbonation alteration with a high loss on ignition (7.64–9.68 wt%). The major elements, such as K_2O and Na_2O, are greatly affected by the alteration; therefore, the REEs and trace elements are mainly used for analysis in this paper.

The andesitic porphyrite is enriched in LILEs (such as Rb, U, and K) and LREEs but depleted in HREEs and HFSEs (such as Nb, Ta, and Ti). The main formation mechanisms for these features include the partial melting of crustal materials, partial melting of mantle-derived materials accompanied by strong crustal contamination, and partial melting of enriched mantle formed by fluid/melt metasomatism in the subduction zone.

The low SiO_2 content (average 57.36 wt%) of andesitic porphyrite suggests that it cannot have been derived from the partial melting of crustal materials. Nb/U, Ta/U, and Ce/Pb can usually be used as indicators to judge crustal contamination. The Nb/U, Ta/U, and Ce/Pb ratios of the samples are 6.2, 0.3 and 4.6, respectively, which are lower than the crustal values (Nb/U = 12.1, Ta/U = 1.1, and Ce/Pb = 4.1) (Taylor and McLennan 1995) (except that the Ce/Pb values of andesitic porphyrite are higher than the Ce/Pb crustal values). Therefore, large-scale crustal contamination may not have occurred during the formation of the andesitic porphyrite. However, considering the ancient zircons found in the andesitic porphyrite, we consider that these zircons were captured during magma ascent. The formation of andesitic porphyrite involved contamination by crustal materials, but the degree of contamination was low. The andesitic porphyrite shows REE characteristics, trace element patterns and isotope geochemistry similar to those of the Permian monzonite, which indicates that the former may have also been formed by the partial melting of mantle metasomatized by subducted sediment.

6.2 Tectonic evolution

Tectonic evolution can be recorded by the compositions of associated magmatic rocks, so we can reconstruct the tectonic history of the study area and provide support for tectonic evolution in the northern margin of the NCC by the rock assemblages outlined above.

6.2.1 *Late Silurian and Middle Permian subduction*

As mentioned above, both Late Silurian gabbroic diorite and Middle Permian monzonite have geochemical characteristics of volcanic arc magmatic rocks, indicating a subduction background. The points are located in the

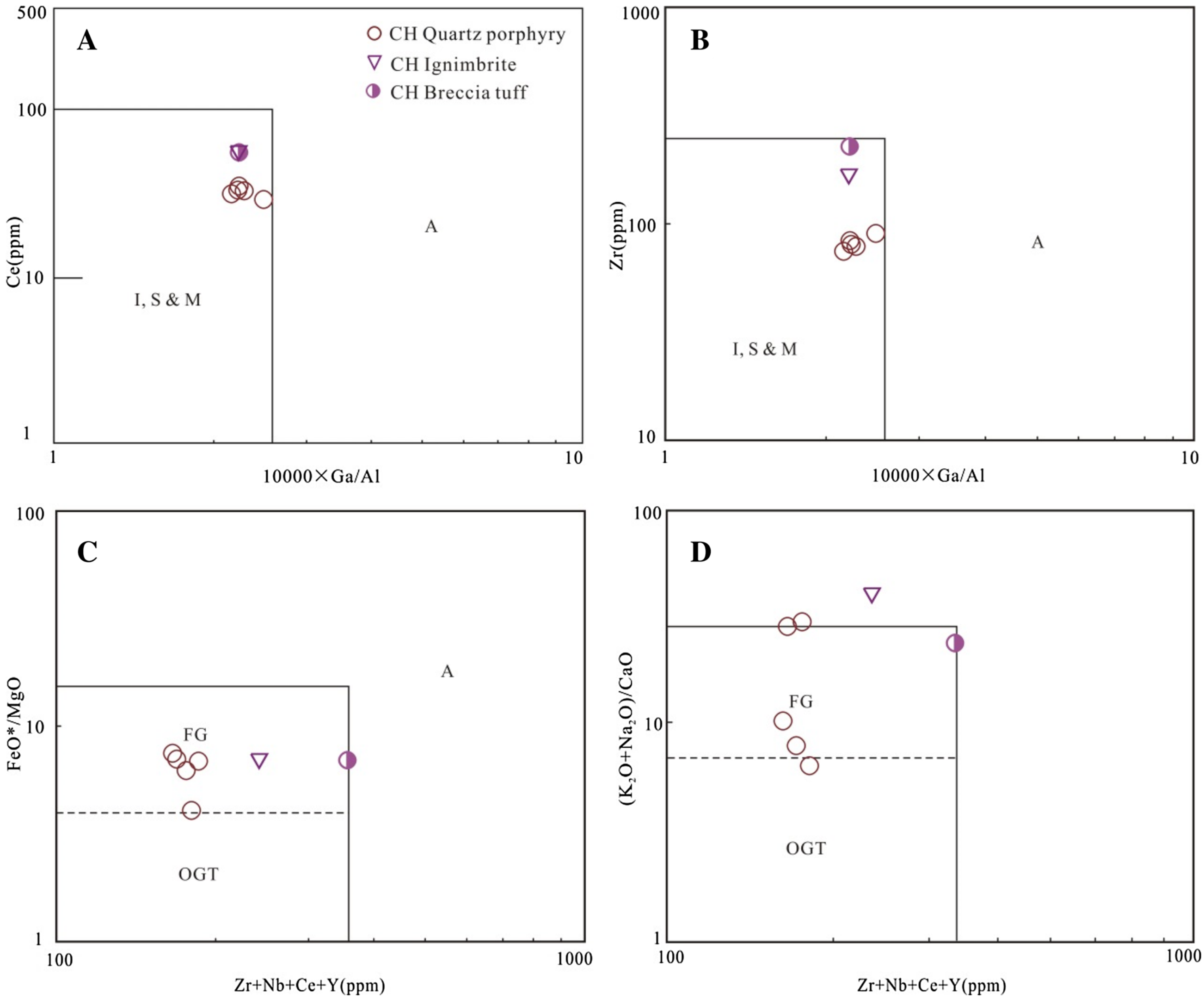

Fig. 11 Ce- and Zr-10,000*Ga/Al (**a**, **b**) and FeO*/MgO- and (K_2O + Na_2O)/CaO–Zr + Nb + Ce + Y (**c**, **d**) diagrams for the quartz porphyry of the Changhanboluo mining area (after Whalen et al. 1987). I S M, I-, S-, and M-type granites, respectively; FG, fractionated I-type granites; OGT, unfractionated I-, S- and M-type granites

volcanic arc field in the discrimination of trace element maps (Fig. 12a, b), and in the La/Nb-Ba/Nb diagram, the samples are also located in the arc volcanic field (Fig. 12c). The HFSE ratios with Yb normalization can reduce the effects of partial melting and fractional crystallization, so these ratios should closely reflect the source region characteristics. The Th/Yb-Nb/Yb diagram distinguishes continental arc magmas from oceanic arc magmas (Pearce and Peate 1995). In Fig. 12d, the gabbroic diorite and monzonite samples are all located in the continental arc area. Therefore, the Late Silurian and Permian magmatic rocks in this area are most likely to have formed against a continental arc background, which was related to the subduction of the Paleo-Asian Ocean Plate beneath the North China Plate.

The northern margin of the NCC underwent a long geological evolution process from the Paleozoic to Mesozoic (Meng 2003; Xiao et al. 2003; Liu et al. 2005). Late Paleozoic granitoids are also abundant along the northern margin of the NCC. They range from gabbro, diorite, and granodiorite to tonalite in composition and constitute a plutonic complex that was continuously emplaced from the Late Carboniferous to the Early Permian (324–274 Ma; Zhang et al. 2007a, 2009a, b, c). In the Early Paleozoic, the Paleo-Asian Ocean subducted beneath the North China Block and formed the Early Paleozoic arc accretion series (490–446 Ma) (Xiao et al. 2003; Windley et al. 2007). With the continued subduction of the Paleo-Asian Ocean, the Dongzi gabbroic diorite was formed in the subduction setting. During the Middle-Late Paleozoic, Andean-type continental arc magmatism (390–270 Ma; Zhang et al.

2007b, c, 2009a) developed on the northern margin of the NCC. The monzonite was formed against the Permian subduction background, and the source may have been a mantle zone metasomatized by melt released from the subducting plate. The Permian mineralization in the northern margin of the NCC formed deposits such as Haolibao, Chehugou, Hadamiao, and Bilihe. Among them, the Re–Os isochron age of molybdenite in the Haolibao deposit is 265 Ma (Zeng et al. 2013); the Rb–Sr isochron age of veinlet chalcopyrite in the Chehugou deposit is 256 Ma (Wan et al. 2009); and the Re–Os weighted mean age and isochron age of molybdenite are 258 and 250 Ma, respectively (Liu et al. 2010; Meng et al. 2013). The zircon LA-ICP-MS U–Pb age of the ore-forming porphyry in the Hadamiao gold deposit is 271 Ma (Lu et al. 2009); the Re–Os isochron age of molybdenite in the Bilihe gold deposit is 273 Ma (Qing et al. 2011), and the zircon U–Pb isotope age of the granodiorite porphyry-monzogranite porphyry is 284–280 Ma (Lu et al. 2012). These Late Paleozoic metallogenic events provide evidence for the Late Paleozoic convergent plate tectonic system in the northern margin of the NCC and establish a theoretical foundation for the exploration of Late Paleozoic deposits.

6.2.2 *Late Jurassic collision*

Late Jurassic magmatism mainly formed ignimbrites, breccia tuffs, quartz monzonite porphyry veins and quartz porphyry veins in this area. The rocks may have been formed against the background of crustal thickening in a syncollisional stage or an early postcollisional stage. Li et al. (2007) noted that the collision between the North China Plate and the Siberian Plate occurred in the Middle and Late Permian and probably lasted to the Middle

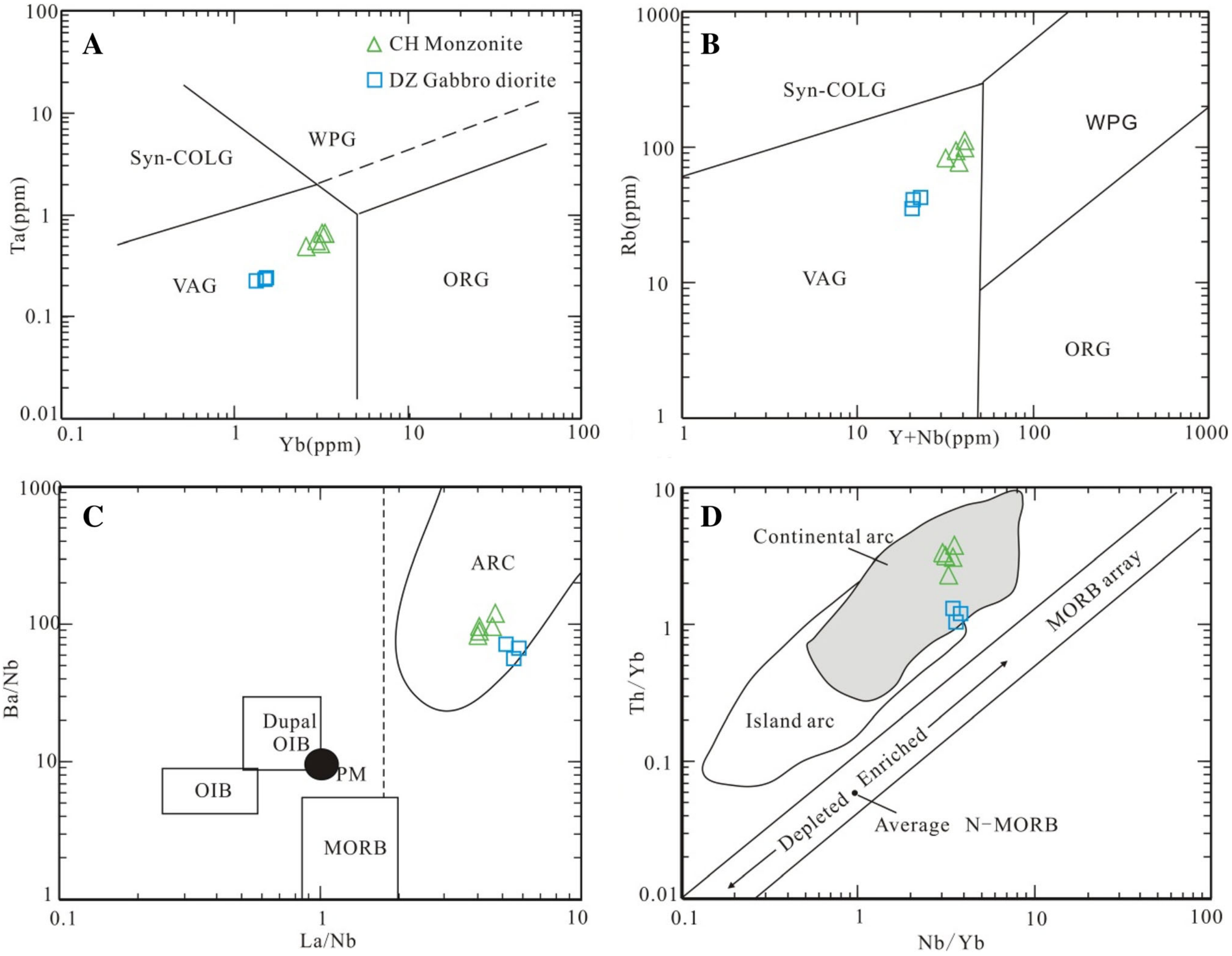

Fig. 12 Discrimination diagrams of the tectonic setting for the gabbroic diorite and monzonite. **a** Diagram of Yb versus Ta (after Pearce et al. 1984); **b** diagram of Y + Nb versus Rb (after Pearce 1996); **c** diagram of Ba/Nb versus La/Nb (after Jahn et al. 1999; Fan et al. 2004); **d** diagram of Nb/Yb versus Th/Yb (after Pearce and Peate 1995). Abbreviations: syn-COLG, syncollisional granites; VAG, volcanic arc granites; ORG, oceanic ridge granites; WPG, within-plate granites; Dupal OIB, ocean island basalts with Dupal anomaly

Triassic, which may have been a relatively long geological process. The mingling of all kinds of ancient animals in the middle Permian marked the beginning of the collision. The appearance of molasse deposits in the Early-Middle Triassic and the occurrence of magmatism in the Middle Triassic indicated the occurrence and end of the collision, respectively. Zhang et al. (2009a) also noted that the final collision between the North China Plate and the Siberian Plate may have occurred between 270 and 250 Ma. Wan et al. (2009) claimed that the closure of the Paleo-Asian Ocean north of the Chifeng area may have occurred before 260 Ma, possibly during the Middle Permian. Therefore, we infer that the northern margin of the NCC may have been in a post-collisional setting during the Late Jurassic (153–158 Ma), with no obvious crustal thinning. The extension stage and compression-extension transition stage of post-collision are the peak periods of large-scale mineralization (Wang and Xu 2006). Since the Early and Middle Jurassic, the northern margin of the NCC has been in the transitional system between the Paleo-Asian Ocean tectonic domain and the Paleo-Pacific Ocean tectonic domain. Under the influence of multidirectional tectonic stresses, strong magmatic activity developed, accompanied by a large number of polymetallic deposits (Wu and Sun 1999; Mao et al. 2005; Zhang et al. 2010b), such as the Jiguanshan molybdenum deposit and Nianzigou molybdenum deposit. Among them, the Re–Os isochron age of the Jiguanshan porphyry molybdenum deposit is 155 Ma (Wu et al. 2011), while the Re–Os isochron age of the Nianzigou quartz vein molybdenum mineralized deposit is 154 Ma (Zhang et al. 2009d), which means that both formed in the postorogenic extensional tectonic setting (Chen et al. 2008). Most deposits in the Shaolanghe Pb–Zn–Ag metallogenic belt were formed in the Jurassic, and the formation of deposits may have been related to magmatism in this period.

6.2.3 Early Cretaceous extension

The regional tectonic system in the northern margin of the NCC has undergone an important transformation (Zhao et al. 2004) from an E-W-trending tectonic system in the Early Mesozoic to a NE- to NNE-trending system in the Late Mesozoic-Early Cenozoic. For example, Ren et al. (1997) found that the E-W-trending Middle-Late Jurassic Tiaoijishan Formation volcanic rocks and the Tuchengzi Formation red strata discovered in northern Hebei and southern Inner Mongolia are overlapped by the NE- to NNE-trending Early Cretaceous Zhangjiakou Formation and Yixian Formation volcanic rocks, which suggests that the Jurassic-Cretaceous was an important transitional period for the dynamic structure in the eastern part of the NCC. In addition, many NE- to NNE-trending faults have been formed. Li (2013) believed that the time of transition from an E-W to a NE-NNE tectonic system in eastern China was 143–120 Ma. The Cretaceous andesitic porphyrite may have been formed against the background of lithospheric extension and thinning. The upwelling of asthenospheric mantle and the increase in the geothermal gradient resulted in the partial melting of the low-temperature melting components (water and LILE-enriched metasomatic mantle) in the upper lithospheric mantle. During the Cretaceous Period, the northern margin of the NCC underwent intense mineralization and formed deposits such as Xiaodonggou and Hongshanzi. The Xiaodonggou deposit formed at 135 Ma, while the Hongshanzi deposit formed at 132 Ma (Nie et al. 2007). In the northern part of the Xilamulun fault, many Mo and Sn polymetallic deposits have also been found, such as Banlashan, Haolibao, Aolunhua, Huanggang, and Anle. Among these deposits, the age of metallogenic granodiorite in the Banlaishan deposit is 132–133 Ma (Zeng and Liu 2010; Zhang et al. 2010d), the molybdenite Re–Os isochron age of the Aolunhua deposit is 129–132 Ma (Shu et al. 2009; Ma et al. 2009), the molybdenite Re–Os age of the Huanggang deposit is 135 Ma (Zhou et al. 2010), and the age of the Anle deposit is 133 Ma (Wang et al. 2001).

6.3 The relationship with metallogenesis

The Dongzi and Changhanboluo Pb–Zn deposits are located south of the Shaolanghe fault. The ore bodies are obviously controlled by the faults and mainly occur in veins. The ore types are mainly massive, banded, and breccia. The metallic minerals mainly consist of pyrite, galena, and sphalerite, followed by chalcopyrite, freibergite, arsenopyrite, etc. Nonmetallic minerals mainly include quartz, calcite, muscovite, and feldspar. Wall rock alteration mainly developed on both sides of the ore veins and mostly consists of silicification, sericitization, carbonation, chloritization, and other medium- to low-temperature hydrothermal alterations. Previous studies on fluid inclusions of the two deposits show that the ore-forming fluids were characterized by a low temperature and low salinity (Xie et al. 2016a; Wang et al. 2017). The above geological characteristics show that the Dongzi and Changhanboluo deposits are hydrothermal vein deposits related to magmatism. According to the above studies, at least four stages of magmatism occurred in this area: Late Silurian ($\sim$ 420 Ma), Middle Permian ($\sim$ 274 Ma), Late Jurassic (153–158 Ma), and Early Cretaceous ($\sim$ 127 Ma). Which stage of magmatism was related to the formation of the deposits?

From the geological characteristics, the gabbroic diorite and monzonite in the Dongzi–Changhanboluo mining area are the main host rocks of the ore bodies, but their alteration and mineralization are weak, so they cannot possibly

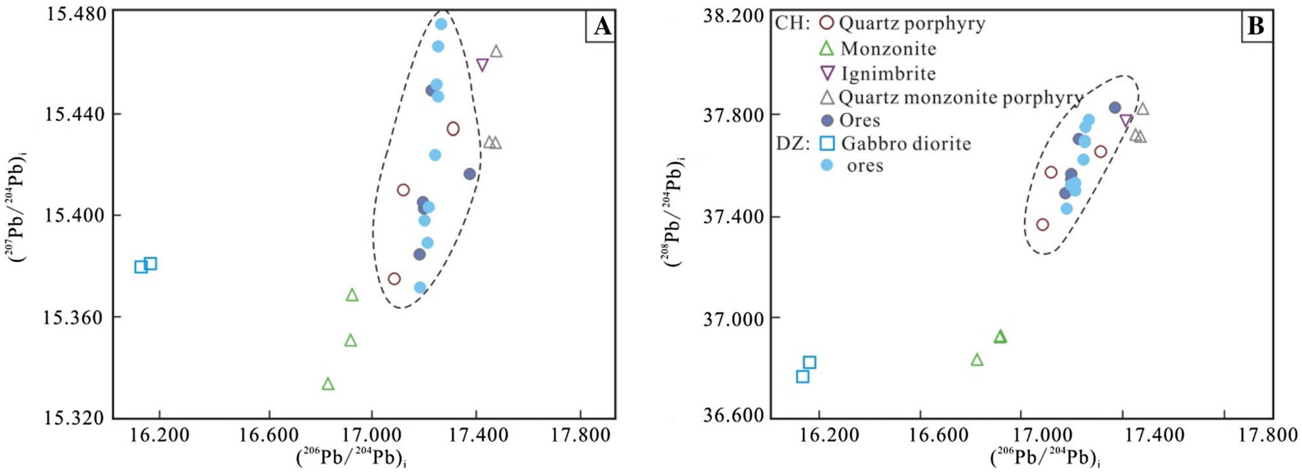

Fig. 13 The $(^{206}\mathrm{Pb}/^{204}\mathrm{Pb})_{\mathrm{i}}$ versus $(^{207}\mathrm{Pb}/^{204}\mathrm{Pb})_{\mathrm{i}}$ (**a**) and $(^{208}\mathrm{Pb}/^{204}\mathrm{Pb})_{\mathrm{i}}$ (**b**) diagrams for the ores and magmas in the Dongzi–Changhanboluo ore district

be the ore-forming geological bodies of the deposits. The Early Cretaceous andesitic porphyrite is clearly younger than the deposits and can be seen to cut through ore bodies; therefore, it is not related to mineralization. The Jurassic quartz porphyry is the main host rock in the Changhanboluo mining area, with sericitization and pyritization alteration, which may be closely related to the formation of the deposit. However, in the Dongzi deposit, the main host rock is diorite and andesite with weak alteration. We did not find quartz porphyry with noticeable alteration. Therefore, we speculated that the ore-forming geological body of the Dongzi deposit should be remote Jurassic magmatic rocks. Based on combining this information with the geochronology studies, the ore-forming ages of the Dongzi and Changhanboluo deposits are 153 Ma and 157 Ma (Chen et al. 2003; Xie et al. 2016a), respectively. The gabbroic diorite (420 Ma) and monzonite (274 Ma) were obviously earlier than the ore-forming age of the Dongzi and Changhanboluo deposits, while the Early Cretaceous andesite porphyrite (127 Ma) was obviously later than the ore bodies. Therefore, according to the diagenetic and ore-forming ages, the formation of the deposits was mainly related to the Jurassic magmatism (153–158 Ma). In addition, from the analysis of Pb isotopes (Table 4), the similar Pb isotope ratios of ores from the Dongzi and Changhanboluo deposits indicate that the two deposits have the same metallogenic magma source. The Pb isotope ratios show $(^{206}\mathrm{Pb}/^{204}\mathrm{Pb})_{\mathrm{i}}$ of 17.181–17.374, $(^{207}\mathrm{Pb}/^{204}\mathrm{Pb})_{\mathrm{i}}$ of 15.384–15.476 and $(^{208}\mathrm{Pb}/^{204}\mathrm{Pb})_{\mathrm{i}}$ of 37.425–37.823, which are obviously higher than those of the Dongzi gabbroic diorite and the monzonite batholith [$(^{206}\mathrm{Pb}/^{204}\mathrm{Pb})_{\mathrm{i}}$ of 16.128–16.920, $(^{207}\mathrm{Pb}/^{204}\mathrm{Pb})_{\mathrm{i}}$ of 15.333–15.382, and $(^{208}\mathrm{Pb}/^{204}\mathrm{Pb})_{\mathrm{i}}$ of 36.763–36.923]. The Pb isotope ratios of the ores are similar to those of the Jurassic magmas, such as quartz porphyry, quartz monzonite porphyry and ignimbrite. In Fig. 13, we can see that the Pb isotope ratios of the ores are plotted in the same range as that of quartz porphyry. Therefore, from the comprehensive analysis of geological characteristics, diagenetic and ore-forming ages and Pb isotopes, the formation of ore bodies in the Dongzi–Changhanboluo ore district was closely related to the Jurassic quartz porphyry.

7 Conclusions

Based on the zircon U–Pb ages and the element and isotope geochemical data presented above, we draw the following conclusions:

1. The zircon U–Pb dating identifies four stages of magmatism in the Dongzi–Changhanboluo ore district: Late Silurian gabbro diorite (~ 420 Ma), Middle Permian quartz monzonite (~ 274 Ma), Late Jurassic quartz porphyry, ignimbrite and breccia tuff (153–158 Ma), and Early Cretaceous andesitic porphyrite (~ 127 Ma).
2. The gabbroic diorite may have been sourced from EM1-type mantle. The monzonite source may have been a mantle zone of metasomatism from fluid/melt released by the subducting plate. The Jurassic volcaniclastic rocks were sourced from the partial melting of the sedimentary rocks. Quartz monzonite porphyry and quartz porphyry formed from the partial melting of a mantle source area metasomatized by subducted sediments, but the quartz porphyry experienced high-degree of differentiation and evolution. The andesite porphyrite has characteristics similar to those of the

Permian monzonite sourced from a mantle zone metasomatized by subducted sediment.

3. The late Silurian and Permian magmatic rocks in this area most likely formed against a continental margin arc background, which was related to the subduction of the Paleo-Asian Ocean Plate beneath the North China Plate. The Late Jurassic magmatic rocks suggest that the northern margin of the NCC may have been in a post-collisional setting during the Late Jurassic, with no obvious crustal thinning. The Cretaceous andesite porphyrite may have been formed against the background of lithospheric extension and thinning.
4. According to the comprehensive analysis of geological characteristics, diagenetic and metallogenic epochs and Pb isotope data, the formation of ore bodies in the Dongzi–Changhanboluo ore district was closely related to the Jurassic quartz porphyry.

Acknowledgements We thank the two anonymous reviewers for their constructive comments that helped improve the manuscript. This work was financially supported by the National Natural Science Foundation of China (No. 41602101).

References

Boynton WV (1984) Cosmochemistry of the rare earth elements: meteorite studies. In: Henderson P (ed) Rare earth elements geochemistry. Elsevier, Amsterdam, pp 63–114

Chappel BW, White AJR (1974) Two contrasting granite types. Pac Geol 8:173–174

Chen YC, Xue CJ, Wang DH, Li HQ, Lu YF (2003) A discussion on the regional mineralizing pedigree of the ore deposits in the northern margin of the North China Landmass. Geol J China Univ 9(4):520–535 **(in Chinese with English abstract)**

Chen ZG, Zhang LC, Wu HY, Wan B, Zeng QD (2008) Geochemistry study and tectonic background of A style host granite in Nianzigou molybdenum deposit in Xilamulun molybdenum metallogenic belt, Inner Mongolia. Acta Pet Sin 24(4):879–889 **(in Chinese with English abstract)**

Chung SL, Wang KL, Crawford AJ, Kamenetsky VS, Chen CH, Lan CY, Chen CH (2001) High-Mg potassic rocks from Taiwan: implications for the genesis of orogenic potassic lavas. Lithos 59:153–170

Clemens JD, Holloway JR, White AJR (1986) Origin of an A-type granite: experimental constraints. Am Miner 71:317–324

Defant MJ, Drummond MS (1990) Derivation of some modern arc magmas by melting of young subducted lithosphere. Nature 347:662–665

Deng JF, Luo ZH, Su SG, Mo XX, Yu BS, Lai XY (2004) Petrogenesis, tectonic environment and mineralization. Geological Publishing House, Beijing, pp 1–381 **(in Chinese)**

Eklund O, Konopelko D, Rutanen H, Frojdo S, Shebanov AD (1998) 1.8 Ga Svecofennian post-collisional shoshonitic magmatism in the Fennoscandian shield. Lithos 45:87–108

Fan WM, Guo F, Wang YJ, Zhang M (2004) Late Mesozoic volcanism in the northern Huaiyang tectonic-magmatic belt, central China: partial melts from a lithospheric mantle with subducted continental crust relicts beneath the Dabie orogen? Chem Geol 209:27–48

Fitton JG, James D, Kempton PD, Ormerod DS, Leeman WP (1988) The role of lithosphere mantle in the generation of Late Cenozoic basic magmas in the western United States. J Petrol 1:331–349

Foley SF, Peccerillo A (1992) Potassic and ultrapotassic magmas and their origin. Lithos 28:181–185

Fowler MB, Henney PJ (1996) Mixed Caledonian appinite magmas: implications for lamprophyre fractionation and high Ba–Sr granite genesis. Contrib Miner Petrol 126:199–215

Han BF, Wang SG, Jahn BM, Hong DW, Kagami H, Sun YL (1997) Depleted-mantle source for the Ulungur River A-type granites, from North Xinjiang, China: geochemistry and Nd–Sr isotopic evidence, and implications for Phanerozoic crustal growth. Chem Geol 138:135–159

Hoskin PWO, Black LP (2000) Metamorphic zircon formation by solidstate recrystallization of protolith igneous zircon. J Metamorph Geol 18(4):423–439

Irvine TH, Baragar WRA (1971) A guide to the chemical classification of the common volcanic rocks. Can J Earth Sci 8:523–548

Jahn BM, Wu FY, Lo CH, Tsai CH (1999) Crust–mantle interaction induced by deep subduction of the continental crust: geochemical and Sr–Nd isotopic evidence from post-collisional maficultramafic intrusions of the northern Dabie complex, central China. Chem Geol 157:119–146

King PL, White AJR, Chappell BW, Allen CM (1997) Characterization and origin of aluminous A-type granites from the Lachlan Fold Belt, Southeastern Australia. J Petrol 38:371–391

Koschek G (1993) Origin and significance of the SEM cathodoluminescence from zircon. J Microsc 171:223–232

Leat PT, Thompson RN, Morrison MA, Hendry GL, Dickin AP (1988) Compositionally-diverse miocene-recent rift-related magmatism in northwest Colorado: partial melting, and mixing of mafic magmas from 3 different asthenospheric and lithospheric mantle sources. J Petrol 1:351–377

Li ZK (2013) Metallogenesis of the silver-lead-zinc deposits along the southern margin of the North China Craton. China University of Geosciences, Wuhan, pp 1–197 **(in Chinese with English abstract)**

Li XH, Zhou HW, Liu Y, Lee CY, Chen CH, Yu JS, Gui XT (2001) Mesozoic shoshonitic intrusives in the Yangchun Basin, western Guangdong, and their tectonic significance: II. Trace elements and Sr–Nd isotopes. Geochimica 30(1):57–65

Li Y, Wu TR, Luo HL, Zhao L (2006) Geochemistry and tectonic setting of the Early Cretaceous shoshonite of Siziwangqi area, Inner Mongolia. Acta Pet Sin 22(11):2791–2800 (**in Chinese with English abstract**)

Li JY, Gao LM, Sun GH, Li YP, Wang YB (2007) Shuangjingzi Middle Triassic syn-colisional crust-derived granite in the east Inner Mongolia and its constraint on the timing of collision between Siberian and Sino-Korean paleo-plates. Acta Pet Sin 23(3):565–582 **(in Chinese with English abstract)**

Li XH, Liu Y, Li QL, Guo CH, Chamberlain KR (2009) Precise determination of Phanerozoic zircon Pb/Pb age by multicollector SIMS without external standardization. Geochem Geophys Geosyst. https://doi.org/10.1029/2009gc002607

Li XW, Mo XX, Bader T, Scheltens M, Yu XH, Dong GC, Huang XF (2014) Petrology, geochemistry and geochronology of the magmatic suite from the Jianzha Complex, central China: petrogenesis and geodynamic implications. J Asian Earth Sci 95:164–181

Li XW, Mo XX, Huang XF, Dong GC, Yu XH, Luo MF, Liu YB (2015) U–Pb zircon geochronology, geochemical and Sr–Nd–Hf isotopic compositions of the Early Indosinian Tongren Pluton in West Qinling: petrogenesis and geodynamic implications. J Asian Earth Sci 97:38–50

Liu HT, Zhai MG, Liu JM, Sun SH (2002) The Mesozoic granitoids in the northern marginal region of North China Craton: evolution from post-collisional to anorogenic settings. Acta Pet Sin 18(4):433–448 **(in Chinese with English abstract)**

Liu W, Siebel W, Li XJ, Pan XF (2005) Petrogenesis of the Linxi granitoids, northern Inner Mongolia of China: constraints on basaltic underplating. Chem Geol 219:5–35

Liu JM, Zhao Y, Sun YL, Li DP, Liu J, Chen BL, Zhang SH, Sun WD (2010) Recognition of the Latest Permian to Early Triassic Cu–Mo mineralization on the north margin of the North China block and its geological significance. Gondwana Res 17:125–134

Liu ZF, Shao YJ, Zhou X, Zhang Y, Zhou GB (2014) Hydrogen, oxygen, sulfur and lead isotope composition tracing for the oreforming material source of Dongguashan copper (gold) deposit in Tongling, Anhui Province. Acta Pet Sin 30(1):199–208 **(in Chinese with English abstract)**

Lu YH, Li WB, Zhong RC, Lai Y (2009) Time and tectonic setting of hosting porphyry of the Hadamiao gold deposit in Xianghuangqi, Inner Mongolia. Acta Pet Sin 25(10):2615–2620 **(in Chinese with English abstract)**

Lu YM, Pan M, Qing M, Zhang YJ, Han XJ, Chao YY (2012) Zircon U–Pb age of gold-bearing granitic intrusive rocks in Bilihe gold deposit of Inner Mongolia and its geological significance. Acta Pet Sin 28(3):993–1004 **(in Chinese with English abstract)**

Ludwig KR (2003) User's manual for ISOPLOT 3.00: a geochronological toolkit for Microsoft Excel. Berkeley Geochronology Center Special Publication, Berkeley, pp 41–70

Lugmair GW, Marti K (1978) Lunar initial 143Nd/144Nd: differential evolution of the lunar crust and mantle. Earth Planet Sci Lett 39:349–357

Ma XH, Chen B, Lai Y, Lu HY (2009) Petrogenesis and mineralization chronology study on the Aolunhua porphyry Mo deposit, Inner Mongolia, and its geological implications. Acta Pet Sin 25(11):2939–2950 **(in Chinese with English abstract)**

Maniar PD, Piccoli PM (1989) Tectonic discrimination of granitoids. Geol Soc Am Bull 101:635–643

Mao JW, Xie GQ, Zhang ZH, Li XF, Wang YT, Zhang CQ, Li YF (2005) Mesozoic large-scale metallogenic pulses in North China and corresponding geodynamic settings. Acta Pet Sin 21(1):169–188 **(in Chinese with English abstract)**

Martin H, Smithies RH, Rapp R, Moyen JF, Champion D (2005) An overview of adakite, tonalite–trondhjemite–granodiorite (TTG), and sanukitoid: relationships and some implications for crustal evolution. Lithos 79:1–24

McDonough WF, Sun SS, Ringwood AE, Jagoutz E, Hofmann AW (1992) Potassium, rubidium, and cesium in the Earth and Moon and the evolution of the mantle of the Earth. Geochim Cosmochim Acta 56:1001–1012

Meng QR (2003) What drove late Mesozoic extension of the northern China–Mongolia tract? Tectonophysics 369:155–174

Meng S, Yan C, Lai Y, Shu QH, Sun Y (2013) Study on the mineralization chronology and characteristics of mineralization fluid from the Chehugou porphyry Mo–Cu deposit, Inner Mongolia. Acta Pet Sin 29(1):255–269 **(in Chinese with English abstract)**

Morrison GW (1980) Characteristics and tectonic setting of the shoshonite rock association. Lithos 13:97–108

Muller D, Groves DI (1995) Potassic igneous rocks and associated gold-copper mineralization. Springer, Berlin, pp 1–144

Nie FJ, Zhang WY, Du AD, Jiang SH, Liu Y (2007) Re–Os isotopic dating on molybdenite separates from the Xiaodonggou porphyry Mo deposit, Hexigten Qi, Inner Mongolia. Acta Geol Sin 81(7):898–905 **(in Chinese with English abstract)**

Pearce JA (1996) Source and settings of granitic rocks. Episodes 19:120–125

Pearce JA, Peate DW (1995) Tectonic implications of the composition of volcanic arc magma. Annu Rev Earth Planet Sci 23:251–285

Pearce JA, Harris NBW, Tindle AG (1984) Trace element discrimination diagrams for the tectonic interpretation of granitic rocks. J Petrol 25:956–983

Peccerillo A, Taylor DR (1976) Geochemistry of eocene calcalkaline volcanic rocks from Kastamonu Area, Northern Turkey. Contrib Mineral Petrol 58:63–91

Qin F, Liu JM, Zeng Q, Luo Z (2009) Petrogenetic and metallogenic mechanism of the Xiaodonggou porphyry molybdenum deposit in Hexigten Banner, Inner Mongolia. Acta Pet Sin 25:3357–3368 **(in Chinese with English abstract)**

Qing M, Ge LS, Tang MG, Qu WJ, Yuan SS, Zhao YS (2011) Molybdnite Re–Os isotope age of Bilihe large-size porphyry gold deposit in Sunid Right Banner of Inner Mongolia and its geological significance. Miner Depos 30(1):11–20 **(in Chinese with English abstract)**

Rapp RP, Watson EB (1995) Dehydration melting of metabasalt at 8–32 kbar: implications for continental growth and crust–mantle recycling. J Petrol 36:891–932

Rapp RP, Watson EB, Miller CF (1991) Partial melting of amphibolite/eclogite and the origin of Archaean trondhjemites and tonalites. Precambrian Res 51:1–25

Ren JS, Niu BG, He ZJ, Xie GL, Liu ZG (1997) Tectonic framework and geodynamic evolution of eastern China. Dixue Yanjiu 29–30:43–55 **(in Chinese with English abstract)**

Rui ZY, Shi LD, Fang RH (1994) Geology of non-ferrous deposits in north margin of the North China Craton and its adjacent areas. Geological Publishing House, Beijing, pp 364–382 **(in Chinese with English abstract)**

Shu QH, Jiang L, Lai Y, Lu YH (2009) Geochronology and fluid inclusion study of the Aolunhua porphyry Cu–Mo deposit in Arhorqin area, Inner Mongolia. Acta Pet Sin 25(10):2601–2614 **(in Chinese with English abstract)**

Shu QH, Lai Y, Zhou YT, Xu JJ, Wu HY (2015) Zircon U–Pb geochronology and Sr–Nd–Pb–Hf isotopic constraints on thetiming and origin of Mesozoic granitoids hosting the Mo deposits in northern Xilamulun district, NE China. Lithos 238:64–75

Song SG, Wang MJ, Wang C, Niu Y (2015) Magmatism during continental collision, subduction, exhumation and mountain collapse in collisional orogenic belts and continental net growth: a perspective. Sci China Earth Sci 45:916–940 (**in Chinese with English abstract**)

Springer W, Seck HA (1997) Partial fusion of basic granulites at 5 to 15 kbar: implications for the origin of TTG magmas. Contrib Mineral Petrol 127:30–45

Steiger RH, Jäger E (1977) Subcommission on geochronology; convention on the use of decay constants in geochronology and cosmochronology. Earth Planet Sci Lett 36:359–362

Sun ZJ (2013) Study on gold deposits mineralization in Chifeng-Chaoyang region, northern margin of North China Craton. Jilin University, Jilin, pp 1–194 **(in Chinese with English abstract)**

Sylvester PJ (1998) Post-collisional strongly peraluminous granites. Lithos 45:29–44

Tang YZ (2013) Geological characteristics and genesis of the Dongzi Pb–Zn deposit, Ongniud Bannar, Inner Mongolia. Inner Mongolia Sci Technol Econ 2:45–49 **(in Chinese with English abstract)**

Taylor SR, McLennan S (1995) The geochemical evolution of the continental crust. Rev Geophys 33(2):241–265

Turner S, Arnaud N, Liu J, Rogers N, Hawkesworth C, Harris N, Kelley S, Van Calsteren P, Deng W (1996) Post-collision, shoshonitic volcanism on the Tibetan Plateau: implications for convective thinning of the lithosphere and the source of ocean island basalts. J Petrol 37(1):45–71

Wan B, Hegner E, Zhang LC, Rocholl A, Chen ZG, Wu HY, Chen FK (2009) Rb–Sr geochronology of chalcopyrite from the Chehugou porphyry Mo–Cu deposit (Northeast China) and geochemical constraints on the origin of hosting granites. Econ Geol 104:351–363

Wang CG (2016) Study on metallogenesis of lead-zinc polymetallic deposit in Shanglang River metallogenic belt, Inner Mongolia. Jinlin University, Jilin, pp 1–192 **(in Chinese with English abstract)**

Wang JB, Xu X (2006) Post-collisional tectonic evolution and metallogenesis in northern Xinjiang, China. Acta Geol Sin 1:23–31 **(in Chinese with English abstract)**

Wang JB, Wang YW, Wang LJ, Uemoto T (2001) Tin-polymetallic mineralization in the southern part of the Da Hinggan Mountains, China. Res Geol 51(4):283–291

Wang CG, Sun GS, He X, Wang GW, Ren LM, Li XP, Zhang FY, Dong XJ (2017) Characteristics and genesis of ore-forming fluid in Dongzi Pb–Zn deposit of Wengniute Banner, Inner Mongolia. Glob Geol 36(4):1116–1123 **(in Chinese with English abstract)**

Watson EB, Harrison TM (1983) Zircon saturation revisited: temperature and composition effects in a variety of crustal magma types. Earth Planet Sci Lett 64:295–304

Weaver BL (1991) The origin of ocean island basalt end-member compositions: trace element and isotopic constraints. Earth Planet Sci Lett 104:381–397

Whalen JB, Currie KL, Chappell BW (1987) A-type granites: geochemical characteristics, discrimination and petrogenesis. Contrib Mineral Petrol 95:407–419

Wiedenbeck M, Alle P, Corfu F, Griffin WL, Meier M, Oberli F, Vonquadt A, Roddick JC, Speigel W (1995) Three natural zircon standards for U–Th–Pb, Lu–Hf, traceelement and REE analyses. Geostand Newslett 19:1–23

Windley BF, Alexelev D, Xiao WJ, Kroner A, Badarch G (2007) Tectonic models for accretion of the Central Asian Orogenic Belt. J Geol Soc 164:31–47

Wu FY, Sun DY (1999) The Mesozoic magmatism and lithospheric thinning in eastern China. J Changchun Univ Sci Technol 29(4):313–318 **(in Chinese with English abstract)**

Wu HY, Zhang LC, Wan B, Chen ZG, Xiang P, Pirajno F, Du AD, Qu WJ (2011) Re–Os and ^{40}Ar/^{39}Ar ages of the Jiguanshan porphyry Mo deposit, Xilamulun metallogenic belt, NE China, and constraints on mineralization events. Miner Depos 46:171–185

Wu HY, Zhang LC, Pirajno F, Xiang P, Wan B, Chen ZG, Zhang XJ (2014) The Jiguanshan porphyry Mo deposit in the Xilamulun metallogenic belt, northern margin of the North China Craton, U–Pb geochronology, isotope systematic, geochemistry and fluid inclusion studies: implications for a genetic model. Ore Geol Rev 56:549–565

Xia B, Lin QC, Zhang YQ (2006) Qinghai-Tibet plateau and its genesis and geological implications. Acta Geol Sin 80(8):1189–1195 **(in Chinese with English abstract)**

Xiao WJ, Windley BF, Hao J, Zhai M (2003) Accretion leading to collision and the Permian Solonker suture, Inner Mongolia, China: termination of the central Asian orogenic belt. Tectonics 22:1484–1505

Xie HJ, Wang YW, Jiang W, Zhang YG, Sun ZY, Kou HC (2016a) Geological characteristics and genesis of the Dongzi Pb–Zn deposit, Inner Mongolia. Miner Explor 7(1):82–92 **(in Chinese with English abstract)**

Xie HJ, Wang YW, Wang LJ, Jiang W, Zhang YG, Kou HC, Sun ZY (2016b) Fluid inclusions study of the Changhanboluo Pb–Zn–Ag deposit, Inner Mongolia. Geol China 43(2):531–545 **(in Chinese with English abstract)**

Xiong XL, Adam J, Green TH (2005) Rutile stability and rutile/melt HFSE partitioning during partial melting of hydrous basalt: implications for TTG genesis. Chem Geol 218(3–4):339–359

Zeng QD, Liu JM (2010) Zircon SHRIMP U–Pb dating and geological significance of the granite porphyry from Banlashan porphyry molybdenum deposit in Xilamulun molybdenum metallogenic belt. J Jilin Univ (Earth Sci Ed) 40(4):828–834

Zeng QD, Sun Y, Duan XX, Liu JM (2013) U–Pb and Re–Os geochronology of the Haolibao porphyry Mo–Cu deposit, NE China: implications for a Late Permian tectonic setting. Geol Mag 150:975–985

Zhang Q, Wang Y, Li CD, Wang YL, Jin WJ, Jia XQ (2006) Granite classification on the basis of Sr and Yb contents and its implications. Acta Pet Sin 22(9):2249–2269 **(in Chinese with English abstract)**

Zhang SH, Zhao Y, Song B, Yang ZY, Hu JM, Wu H (2007a) Carboniferous granitic plutons from the northern margin of the North China block: implications for a late Palaeozoic active continental margin. J Geol Soc 164:451–463

Zhang SH, Zhao Y, Liu J, Hu JM, Chen ZL, Li M, Pei JL, Chen ZY, Zhou JX (2007b) Emplacement depths of the Late Paleozoic to Mesozoic granitoid intrusions from the northern North China block and their tectonic implications. Acta Pet Sin 23:625–638 **(In Chinese with English abstract)**

Zhang SH, Zhao Y, Song B, Yang YH (2007c) Zircon SHRIMP U–Pb and in situ Lu–Hf isotope analyses of a tuff from western Beijing: evidence for missing Late Paleozoic arc volcano eruptions at the northern margin of the North China block. Gondwana Res 12:157–165

Zhang SH, Zhao Y, Kröner A, Liu XM, Xie LW, Chen F (2009a) Early Permian plutons from the northern North China Block: constraints on continental arc evolution and convergent margin magmatism related to the Central Asian Orogenic Belt. Inter J Earth Sci 98:1441–1467

Zhang SH, Zhao Y, Liu XC, Liu DY, Chen F, Xie LW, Chen HH (2009b) Late Paleozoic to Early Mesozoic mafic–ultramafic complexes from the northern North China Block: constraints on the composition and evolution of the lithospheric mantle. Lithos 110:229–246

Zhang SH, Zhao Y, Song B, Hu JM, Liu SW, Yang YH, Chen F, Liu XM, Liu J (2009c) Contrasting Late Carboniferous and Late Permian-Middle Triassic intrusive suites from the northern margin of the North China craton: geochronology, petrogenesis, and tectonic implications. Geol Soc Am Bull 121:181–200

Zhang ZL, Zeng QD, Qu WJ, Liu JM, Sun XG, Zhang RB, Chen WJ, Qin F (2009d) The molybdenite Re–Os dating from the Nianzigou Mo deposit, Inner Mongolia and its geological significance. Acta Pet Sin 25(1):212–218 **(in Chinese with English abstract)**

Zhang LC, Wu HY, Xiang P, Zhang XJ, Chen ZG, Wan B (2010a) Ore-forming processes and mineralization of complex tectonic system during the Mesozoic: a case from Xilamulun Cu–Mo metallogenic belt. Acta Pet Sin 26(5):1351–1362 **(in Chinese with English abstract)**

Zhang LC, Wu HY, Xiang P, Zhang XJ, Chen ZG, Wan B (2010b) Ore-forming processes and mineralization of complex tectonic system during the Mesozoic: a case from Xilamulun Cu–Mo metallogenic belt. Acta Pet Sin 26:1351–1362 **(in Chinese with English abstract)**

Zhang Q, Jin WJ, Li CD, Wang YL (2010c) Revisiting the new classification of granitic rocks based on whole-rock Sr and Yb contents: index. Acta Pet Sin 26(4):985–1015 **(in Chinese with English abstract)**

Zhang XJ, Zhang LC, Jin XD, Wu HY, Xiang P, Chen ZG (2010d) U–Pb ages, geochemical characteristics and their implications of

Banlashan molybdenum deposit. Acta Pet Sin 26(5):1411–1422 **(in Chinese with English abstract)**

Zhao Y, Zhang SH, Xu G, Yang ZY, Hu JM (2004) The Jurassic major tectonic events of the Yanshanian intraplate deformation belt. Geol Bull China 23(9–10):854–863 **(in Chinese with English abstract)**

Zhou ZH, Lv LS, Feng JR, Li C, Li T (2010) Molybdenite Re–Os ages of Huanggang skarn Sn–Fe deposit and their geological significance, Inner Mongolia. Acta Pet Sin 26(3):67–79 **(in Chinese with English abstract)**

Zou HB, Mary RR, Liu YS, Yao YP, Xu XS, Fan QC (2003) Constraints on the origin of historic potassic basalts from northeast China by U–Th disequilibrium data. Chem Geol 200:89–201